Numerical study of the interaction between a pulsating coated microbubble and a rigid wall. I. Translational motion

M. Vlachomitrou [*] and N. Pelekasis [†]
Department of Mechanical Engineering, University of Thessaly, Leoforos Athinon, Pedion Areos, 38834 Volos, Greece

(Received 16 March 2020; accepted 16 November 2020; published 6 January 2021)

The dynamic response of an encapsulated bubble to an acoustic disturbance in a wall restricted flow is investigated in the context of axial symmetry, when the viscous forces of the surrounding liquid are accounted for. The Galerkin finite element methodology is employed and the elliptic mesh generation technique is used for updating the mesh. The bubble is accelerated towards the wall as a result of the secondary Bjerknes forces and consequently the translational velocity gradually increases in a nearly quadratic fashion as the bubble approaches the wall. Proximity to the wall affects the resonance frequency that is seen to be reduced as the initial distance between the bubble and the wall decreases, as long as the sound amplitude remains below a threshold value that is determined by the onset of parametric shape mode excitation. While the microbubble remains far from the wall an overpressure develops in the upstream region that causes flattening and bending of the shell. However, shell elasticity coupled with viscous shell stresses prevents jet formation. Thus the bubble remains spherical during the expansion phase of the pulsation and deforms mainly in the compressive phase, during which most of the translation takes place due to the reduced added mass effect. As it approaches the wall the maximum overpressure is moved to the downstream pole region and this generates an excess of viscous shell stresses during compression that balance compressive elastic stresses. As a result the latter are attenuated in the downstream region of the shell, in comparison with the bulk of the shell where they are balanced solely by the cross membrane pressure drop, leading to a gradually more pronounced prolate bubble shape. Viscous drag due to the surrounding liquid develops mainly in the bulk of the shell where it is balanced by viscous shell stresses in the tangential stress balance. Over a period of the pulsation it counteracts the Bjerknes force that accelerates the bubble, via a force balance that is almost instantaneously established due to the relatively large shell viscosity. This is in marked difference with the case of rising gas bubbles that acquire oblate shapes as a result of the balance between buoyancy and pressure drag. In the case of coated microbubbles the drag coefficient is seen to obey a law previously obtained for no-slip interfaces for large radial and relatively small translational Reynolds numbers.

DOI: 10.1103/PhysRevFluids.6.013601

I. INTRODUCTION

The dynamic behavior of encapsulated microbubbles, also known as contrast agents, plays a key role in novel biomedical applications involving ultrasound, among which the most important are medical imaging of vital organs and targeted drug delivery. In the former case, gas-filled

[*] mavlacho@uth.gr
[†] pel@uth.gr

microbubbles are used which are able to enhance the ultrasound backscatter and contrast, in comparison with the acoustic signal from nearby tissue, thus producing high quality images [1] as a result of their nonlinear nature as sound scatterers [2]. Targeted molecular imaging has also been developed [3], whereby specific ligands are attached to the membrane to facilitate the adhesion of the microbubble to a specific diseased area in order to provide better contrast enhancement. In a similar fashion, in targeted drug delivery encapsulated microbubbles that carry drugs are attached to the affected site using an appropriate acoustic disturbance and then ruptured via sonication. Alternatively, low amplitude oscillations of coated microbubbles are employed for the transport of large macromolecules towards the cell cytoplasm via generation of transient micropores in nearby cells [4] or via the acoustic microstreaming process [5,6]. In both situations it is essential to resolve the dynamics of the bubble motion as it approaches the wall and the details of the flow that develops in the region between the wall and the bubble shell.

For such flow arrangements experimental studies report that the presence of a nearby boundary accelerates growth of interfacial instabilities and instigates phenomena such as jet formation and, finally, collapse of the bubble [7,8]. The latter experimental studies examine the situation with the coated microbubble pulsating in response to an acoustic disturbance in the vicinity of a boundary. In this fashion microbubble shapes that are asymmetrically deformed in the direction perpendicular to the boundary surface were captured [7,8] while jet formation was observed in the compression [8] and expansion phase of the pulsation [9], respectively. Furthermore, the microbubble was seen to acquire prolate and oblate shapes on an alternating basis during the pulsation in the vicinity of a wall [7].

In order to assess the effect of bubble-wall interaction on the potential for wall adhesion and the onset of trapped pulsations, the translational part of the motion and its impact on bubble velocity, shape, and resonance frequency needs to be investigated. The latter is also essential in distinguishing between freely circulating and trapped microbubbles. The translating motion of two pulsating free bubbles, i.e., without coating, was studied experimentally by Crum [10] as they translate along the axis connecting their centers of mass due to the scattered pressure field from each other. It was thus seen that they accelerate towards each other with a speed that varies with the inverse square of their distance, as a result of an instantaneous balance between secondary Bjerknes force and Stokes drag obtained for a free surface [11]. The accelerating motion of two interacting bubbles due to the secondary Bjerknes forces was studied numerically by Pelekasis and Tsamopoulos [12,13] in the context of potential theory where the validity of the inverse square law was verified as well as the dependence of the bubble speed on the square of the sound amplitude. The emerging shape of accelerating free surface bubbles was seen in the latter studies to resemble a spherical cap with a significantly deformed upstream region. However, simulations could not proceed for very long times due to the onset of parametric shape mode instabilities which, in the absence of any damping mechanism, emerged for relatively small sound amplitudes. Ryskin and Leal [14,15] developed a finite difference method on an orthogonal adaptive mesh in order to solve the Navier-Stokes equation for the motion of a free bubble of radius R_0 inside a Newtonian liquid of density ρ and dynamic viscosity μ under the action of gravity. They were thus able to capture steadily rising bubbles of velocity U with increasingly oblate axisymmetric shapes as the translational Reynolds number, $\mathrm{Re}_T = \rho U 2R_0/\mu$, increases and more pronounced spherical-cap shapes as the Weber number, $\mathrm{We} = 2\rho U^2 R_0/\sigma$ with σ denoting the surface tension, increases, especially for not very large Re_τ. Furthermore, the validity of Moore's prediction for large Re_T and small We$\sim$1, i.e., not severely deformed bubbles, was corroborated. When a particle with a nonslip surface is considered Levich's theory and Moore's correction are no longer valid, Eqs. (1a) and (1b), respectively,

$$c_D \equiv \frac{\text{dragforce}}{\frac{1}{2}\rho U^2 \pi R_0^2}, \quad c_D = \frac{48}{\mathrm{Re}_T}, \tag{1a}$$

$$c_D = \frac{48}{\mathrm{Re}_T}\left(1 - \frac{2.2}{{\mathrm{Re}_T}^{1/2}}\right) + \mathrm{O}({\mathrm{Re}_T}^{-3/2}), \tag{1b}$$

and experimental [16] as well as theoretical [17] predictions propose an alternative law for the drag coefficient on a pulsating and translating spherical particle:

$$c_D = \frac{24}{\mathrm{Re}_T}\left[1 + 0.15\mathrm{Re}_T^{0.687}\right]. \tag{1c}$$

Equation (1c) constitutes a correction to Stokes' law that is valid when $\mathrm{Re}_T \sim \mathrm{O}(1)$ or larger [17]. It is of interest to examine the dominant components of the force balance as the coated microbubble, which constitutes a nonslip yet deformable interface, accelerates towards the wall.

Extensive numerical simulations of the dynamic response of coated microbubbles are not available in the literature, owing largely to uncertainties regarding proper modeling of the shell, especially in the case of phospholipid shells. Qin and Ferrara [18] developed a lumped parameter model as a means to incorporate elastic effects, mainly in the surrounding vessel, in order to study the acoustic response of a coated microbubble that pulsates in a compliant microvessel. They were thus able to calculate the stresses that develop on the microvessel wall as a result of the pulsating motion, which was also seen to increase the permeability of the vessel. More recently, numerical studies were conducted to address the above issues via the boundary integral [19] and the finite volume [20] method with boundary fitted coordinates, as a means to obtain a more detailed description of the velocity field in the surrounding fluid but also to calculate the elastic stresses on the coating. In particular, Liu *et al.* [20] explored numerically the shape oscillations in an unbounded flow of an encapsulated microbubble that obeys the Mooney-Rivlin constitutive law by solving the continuity and the Navier-Stokes equations with the finite volume method using a boundary fitted coordinate system. They mainly observed subharmonic shape mode excitation when the forcing frequency was twice the natural frequency of the shape mode, in agreement with previous predictions based on linear stability analysis [21]. Tsiglifis and Pelekasis [19] performed boundary integral simulations of pulsating contrast agents, while ignoring viscous effects on the liquid side in view of the relatively large shell viscosity and the typical small size of encapsulated bubbles. They captured harmonic and subharmonic shape mode excitation during the compression phase of the pulsation, for the parameter range predicted by linear stability [21]. This led to saturated shape oscillations and breakup beyond a certain amplitude threshold. The latter response pattern conforms with "dynamic buckling," corresponding to an effect that was identified in [21] as the equivalent of the Rayleigh-Taylor or collapse instability of free bubbles that arises due to the accelerating motion of the interface during the rebound of the compressive phase of the microbubble pulsation. The effect of constitutive law was also examined and it was seen that polymeric bubbles conform well with neo-Hookean behavior whereas phospholipid shells conform with the strain-softening behavior except for the phenomenon of "compression only pulsation." Surface destabilization may also occur before the minimum bubble radius is attained, for large enough negative velocities during collapse as was seen in control volume calculations of laser induced cavitation bubbles [22]. In the latter case interfacial viscosity is not present and very large radial velocities are generated, thus destabilizing the interface during collapse.

Nevertheless, the degree to which potential flow considerations can sufficiently capture the dynamic behavior of deforming contrast agents is not fully understood [19]. Hence, in the present study we investigate numerically the dynamic response of a contrast agent to an acoustic disturbance in a wall restricted flow when the viscous forces of the surrounding liquid are accounted for. We focus on capturing the accelerating motion of the microbubble towards the wall in order to identify the forces that play a key role and control the response. The numerical method that is used is based on a previous work [23] that studied the response of a coated microbubble to a step change disturbance in an unbounded flow and is extended in order to take into account wall presence. Following the latter study, the Galerkin finite element methodology is used and the grid is constructed via the elliptic mesh generation technique since its superiority was clearly demonstrated for large interfacial deformations.

This paper is organized as follows: The problem formulation is discussed in Sec. II A, where the governing equations for the liquid flow are presented along with the ones describing the

encapsulated bubble. The translational motion of the bubble as it approaches the wall is examined and the force balance that determines the bubble speed is identified in Sec. II B. In this context the nature of the so-called secondary Bjerknes forces is analyzed. Next, in Sec. III the numerical method that has been developed for discretizing the governing equations is outlined and the grid construction procedure is described via benchmark simulations, when the microbubble is initially located far from the wall and when it is placed inside a wall restricted flow. In Sec. IV the results of our simulations are presented and the translational motion of the bubble as it performs volume pulsations is investigated, focusing on the evolution of the bubble speed and shape as well as the variation of resonance frequency with decreasing bubble-wall distance. Moreover, the effect of the wall presence in the energy dissipated due to the liquid and shell viscosity is investigated in Appendix. Finally, in Sec. V the main conclusions are summarized and directions for future research are outlined.

II. PROBLEM FORMULATION

A. Governing equations

We are interested in examining the dynamic response to acoustic disturbances of an encapsulated microbubble in a wall restricted flow and to eventually identify conditions that enhance trapped pulsations. The microbubble initial radius is R_0 and is submerged in a Newtonian liquid of density ρ and dynamic viscosity μ. We consider a wall restricted flow, we place the bubble at a certain distance from the wall and investigate the bubble's response to an acoustic disturbance imposed on the far pressure field:

$$P'_\infty = P'_{\rm st} + P'_{\rm dist} = P'_{\rm st} + P'_{\rm st}\varepsilon\cos(\omega_f t'), \tag{2}$$

with $P'_{\rm st}$, $P'_{\rm dist}$ denoting the dimensional undisturbed and disturbed pressure in the far field, respectively; ε the magnitude; and ω_f the frequency of the acoustic disturbance. The initial radius R_0 of the bubble is taken as the characteristic length scale of the problem, the external frequency determines the appropriate timescale as $1/\omega_f$, and the characteristic velocity and pressure scales are set to $\omega_f R_0$ and $\rho\omega_f^2 R_0^2$, respectively. Throughout this paper primed letters signify dimensional variables.

The problem formulation of a contrast agent microbubble in a wall restricted flow is described via a cylindrical coordinate system. In order to obtain the governing equations we assume axisymmetric variations of the bubble shape as well as the liquid velocity and pressure; i.e., no variations are considered in the azimuthal direction for either the liquid or the bubble. In Fig. 1 a schematic representation of the flow under consideration is provided with f_1 denoting the r coordinate of the thin shell that coats the bubble.

The flow in the surrounding liquid is governed by the mass conservation and momentum equations. The liquid is taken to be incompressible in which case the continuity equation and momentum balance, via the Navier-Stokes equations, read in dimensionless form

$$\nabla\cdot\boldsymbol{u} = 0, \tag{3}$$

$$\frac{\partial\boldsymbol{u}}{\partial t} + (\boldsymbol{u}\cdot\nabla)\boldsymbol{u} = -\nabla P + \frac{1}{\mathrm{Re}}\nabla\cdot\underline{\underline{\boldsymbol{\tau}}}, \quad \underline{\underline{\boldsymbol{\sigma}}} = -P\underline{\underline{\boldsymbol{I}}} + \frac{1}{\mathrm{Re}}\underline{\underline{\boldsymbol{\tau}}}, \quad \underline{\underline{\boldsymbol{\tau}}} = \nabla\boldsymbol{u} + \nabla\boldsymbol{u}^T, \tag{4}$$

where $\boldsymbol{u} = (u_r, u_z, 0)$ for the cylindrical coordinate system, $\mathrm{Re} = (\rho\omega_f R_0^2)/\mu$ is the Reynolds number of the surrounding liquid flow that compares inertia with viscous forces, $\underline{\underline{\boldsymbol{\sigma}}}$, $\underline{\underline{\boldsymbol{\tau}}}$ are the full and deviatoric stress tensors in the surrounding fluid, and $\underline{\underline{\boldsymbol{I}}}$ is the unit tensor. In the above formulation buoyancy has been neglected owing to the small size of the bubbles and the flow is treated as incompressible. In order to obtain the deformation of the bubble we use a Lagrangian representation of the interface by introducing a Lagrangian coordinate ξ ($0 \leqslant \xi \leqslant 1$) which identifies the particles

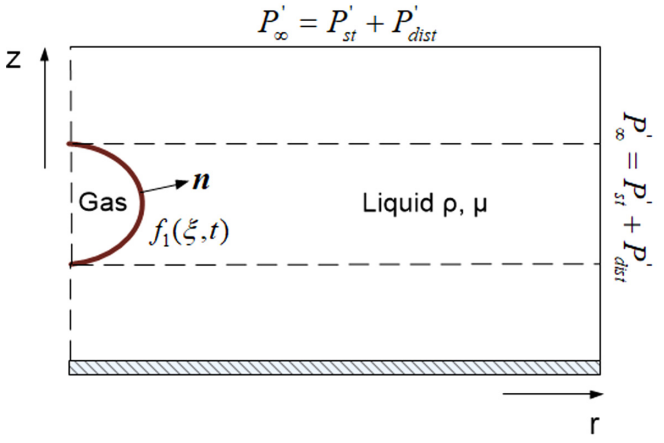

FIG. 1. A contrast agent in a wall restricted flow.

on the interface. In this manner, every interfacial particle is assigned to a different value of ξ with $\xi = 0$ and $\xi = 1$ corresponding to the south and north poles of the bubble, respectively.

The force balance on the gas-liquid interface reads in dimensionless form

$$\left(-P\underline{\underline{\boldsymbol{I}}} + \frac{1}{\mathrm{Re}}\underline{\underline{\boldsymbol{\tau}}}\right)\cdot\boldsymbol{n} + P_G\boldsymbol{n} + \nabla_s\cdot\left[\underline{\underline{\boldsymbol{\tau}}} + \boldsymbol{q}n + \frac{1}{\mathrm{We}}\left(\underline{\underline{\boldsymbol{I}}} - \boldsymbol{nn}\right)\right] = 0$$

$$\xrightarrow[\text{surf tension}]{\text{constant}} \left(-P\underline{\underline{\boldsymbol{I}}} + \frac{1}{\mathrm{Re}}\underline{\underline{\boldsymbol{\tau}}}\right)\cdot\boldsymbol{n} + P_G\boldsymbol{n} = -\nabla_s\cdot\left(\underline{\underline{\boldsymbol{\tau}}} + \boldsymbol{qn}\right) + \frac{2k_m}{\mathrm{We}}\boldsymbol{n} = \boldsymbol{\Delta F} + \frac{2k_m}{\mathrm{We}}\boldsymbol{n}, \tag{5}$$

where $\boldsymbol{n}$ denotes the unit normal vector pointing towards the surrounding fluid and P_G is the pressure of the gas inside the bubble; $\underline{\underline{\boldsymbol{I}}}$, ∇_s, k_m denotes the identity tensor, the surface gradient, and mean curvature of the bubble's interface, respectively, whereas $\mathrm{We} = \frac{\rho\omega_f^2 R_0^3}{\sigma}$ is the Weber number comparing inertia with capillary forces. Despite its viscoelastic nature a certain amount of surface tension, σ, is typically assumed for the shell [24–27] as a measure of the isotropic tension that signifies the degree of exposure of the enclosed gas to the liquid environment. Finally, $\boldsymbol{\Delta F}$ is the resultant force due to the viscoelastic properties of the membrane that is derived by the surface divergence of the viscoelastic tension tensor on the membrane surface:

$$\boldsymbol{\Delta F} = \left[k_s\tau_s + k_\phi\tau_\phi - \frac{1}{r}\frac{\partial}{\partial S}(rq)\right]\boldsymbol{n} - \left[\frac{\partial\tau_s}{\partial S} + \frac{1}{r}\frac{\partial r}{\partial S}(\tau_s - \tau_\phi) + k_s q\right]\boldsymbol{e_s}, \tag{6}$$

with S denoting the arc length of the interface; τ_s, τ_ϕ the principal elastic tensions; k_s, k_ϕ the two principal curvatures; r, z the cylindrical polar and axial coordinates; and $\boldsymbol{e}_s$ the tangential unit vector. q is the transverse shear tension that is obtained from a torque balance on the shell [28,29]:

$$q = \frac{K_B}{r}\frac{\partial r}{\partial S}\left[\frac{\partial}{\partial r}(rm_s) - m_\phi\right], \tag{7a}$$

where m_s, m_ϕ are the principal bending moments and $K_B \equiv k_B/(\rho\omega_f^2 R_0^5)$ signifies the relative importance of bending with respect to inertia. The membrane and bending stresses are defined via the shell constitutive laws. In particular, the transverse shear q points along the normal vector $\boldsymbol{n}$ in a surface that is perpendicular to the tangent vector $\boldsymbol{e}_s$. Finally, the membrane tensions consist of an

elastic and a viscous component, i.e.,

$$\tau_s = \tau_{s,el} + \tau_{s,v}, \quad \tau_s^{\mathrm{MR}} = \frac{G}{3\lambda_s\lambda_\varphi}\left[\lambda_s^2 - \frac{1}{(\lambda_s\lambda_\varphi)^2}\right]\left[1 + b\left(\lambda_\varphi^2 - 1\right)\right] + \frac{2}{\mathrm{Re}_s}\frac{1}{\lambda_s}\frac{\partial\lambda_s}{\partial t}, \tag{7b}$$

$$\lambda_s = \frac{S_\xi(t)}{S_\xi(0)}, \quad \lambda_\phi = \frac{r(t)}{r(0)}, \tag{7c}$$

with λ_s, λ_φ denoting the principal extension ratios and $G \equiv \chi/(\rho\omega_f^2 R_0^3)$ and $\mathrm{Re}_s \equiv \rho\omega_f R_0^3/\mu_s$ signifying the relative importance of shell dilatation and viscosity with respect to inertia. In contrast to the previous study by Vlachomitrou and Pelekasis [23] where the 3 d shell viscosity was signified by μ_s, SI units in Pa s, in the present study μ_s denotes the surface shell viscosity, SI units in kg/s, with $\mu_s = 3\delta\mu_{s,3d}$ where δ is the shell thickness. We adopt the Mooney-Rivlin model for the elastic part with b denoting the degree of shell softness [30] and a linear model for shell viscosity μ_s treating the dilatational and shear viscosity of the shell as equal. A more detailed description of the modeling that is used for the viscoelastic shell of the bubble is given in Tsiglifis and Pelekasis [19,21,31] and Vlachomitrou and Pelekasis [23].

Besides the force balance, continuity of the liquid and shell velocities on the interface reads as

$$\boldsymbol{u} = \frac{D\boldsymbol{r_s}}{Dt}, \tag{8}$$

with $\boldsymbol{r_s} = r\boldsymbol{e}_r + z\boldsymbol{e}_z$ denoting the position vector of a particle at the interface. At equilibrium a stress-free state is assumed on the interface of radius R_0, where the dimensionless pressure P_G inside the bubble is related to the dimensionless pressure P_{st} in the far field through the Young-Laplace equation:

$$P_G(t=0) = P_{\mathrm{st}} + \frac{2}{\mathrm{We}}. \tag{9}$$

The pressure inside the bubble is taken to be uniform due to negligible density and kinematic viscosity of the enclosed gas. Moreover, heat transfer between the bubble and the surrounding liquid is assumed to take place quite fast in comparison with the timescale of the phenomena under consideration. In this context, bubble oscillations are characterized as nearly isothermal and therefore the bubble pressure is given by

$$P_G(t=0)V_G^\gamma(t=0) = P_G(t)V_G^\gamma(t), \tag{10}$$

with V_G denoting the dimensionless instantaneous volume of the bubble, $V_G(t=0) = \frac{4\pi}{3}$ the initial volume of the bubble, and γ the polytropic constant set to 1.07 for an almost isothermal variation. The latter value is also close to the ratio between the specific heats of certain ideal gases that are carried by known contrast agents and undergo adiabatic pulsations during insonation [26,27,31].

B. Radial and translational motion far from the wall

We examine the radial and translational motion of a microbubble that is pulsating in a fluid subject to an acoustic pressure disturbance. In the early stages of the bubble motion and before it reaches the wall it performs radial pulsations with $\mathrm{Re} = \rho\omega_f R_0^2/\mu$. Assuming radial symmetry and invoking linear potential theory for the oscillating bubble, as long as the bubble remains far from resonance, it soon reaches saturation performing a steady pulsation that is described as follows in dimensionless form (see also [31]),

$$P_\infty = P_{\mathrm{st}}[1 + \varepsilon\cos(t)], \quad R(t) = 1 + R_D(t), \quad R_D(t) \ll 1, \tag{11}$$

$$\ddot{R}_D + \left(\frac{4}{\mathrm{Re}} + \frac{4}{\mathrm{Re}_s}\right)\dot{R}_D + \left[3\gamma\left(\frac{2}{\mathrm{We}} + P_{\mathrm{st}}\right) - \frac{2}{\mathrm{We}} + 4G\right]R_D = -\varepsilon P_{\mathrm{st}}\cos t, \tag{12}$$

where R_D is the linear variation of the bubble radius. The above equation admits a particular solution of the form

$$R_D(t) = \varepsilon P_{\rm st} \frac{\left\{1-\left[3\gamma\left(\frac{2}{\rm We}+P_{\rm st}\right)-\frac{2}{\rm We}+4G\right]\right\}\cos t-\left(\frac{4}{\rm Re}+\frac{4}{{\rm Re}_s}\right)\sin t}{\left(\frac{4}{\rm Re}+\frac{4}{{\rm Re}_s}\right)^2+\left\{1-\left[3\gamma\left(\frac{2}{\rm We}+P_{\rm st}\right)-\frac{2}{\rm We}+4G\right]\right\}^2}$$

$$\Rightarrow \frac{R'_D(t)}{R_0} = \varepsilon \frac{P'_{\rm st}}{\rho R_0^2} \frac{\cos(\omega_f t')\left\{\omega_f^2-\left[\frac{3\gamma}{\rho R_0^2}\left(\frac{2\sigma}{R_0}+P'_{\rm st}\right)-\frac{2\sigma}{\rho R_0^3}+4\frac{\chi}{\rho R_0^3}\right]\right\}-\sin(\omega_f t')\omega_f\left(\frac{4\mu}{\rho R_0^2}+\frac{4\mu_s}{\rho R_0^3}\right)}{\omega_f^2\left(\frac{4\mu}{\rho R_0^2}+\frac{4\mu_s}{\rho R_0^3}\right)^2+\left\{\omega_f^2-\left[\frac{3\gamma}{\rho R_0^2}\left(\frac{2\sigma}{R_0}+P'_{\rm st}\right)-\frac{2\sigma}{\rho R_0^3}+4\frac{\chi}{\rho R_0^3}\right]\right\}^2}. \tag{13}$$

It constitutes the final state of steady pulsation corresponding to the complete linear solution that reads as

$$R'_D(t') = A' e^{\omega_r t'}\cos(\omega_i t') + B' e^{\omega_r t'}\sin(\omega_i t') + C'\cos(\omega_f t') + D'\sin(\omega_f t'), \tag{14}$$

and emerges after the initial transient has elapsed. C' and D' are the dimensional equivalents of the coefficients of the sinusoidal functions that arise in Eq. (13); they are related to the actual amplitude of the radial excursion of the microbubble, and strongly depend on the shell properties and the characteristics of the acoustic disturbance. It can be seen that the amplitude of the radial oscillation is much smaller than the nominal value of ε corresponding to the pressure disturbance, especially when the bubble is not excited close to its primary resonance, owing to the shell stiffness and viscosity; an indicative value for the dimensionless amplitude of $R_D(t)$ is $\sim$0.15 for the range of shell parameters employed and a sound amplitude as large as $\varepsilon = 2$. Finally,

$$\omega = \omega_r + i\omega_i, \quad \omega_r = -\left(\frac{2\mu}{\rho R_0^2}+\frac{2\mu_s}{\rho R_0^3}\right),$$

$$\omega_i = \sqrt{\left[\frac{3\gamma}{\rho R_0^2}\left(\frac{2\sigma}{R_0}+P'_{\rm st}\right)-\frac{2\sigma}{\rho R_0^3}+4\frac{\chi}{\rho R_0^3}\right]-4\left(\frac{\mu}{\rho R_0^2}+\frac{\mu_s}{\rho R_0^3}\right)^2} \tag{15}$$

signify the damping rate and eigenfrequency for volume pulsations. It can be easily verified that the type of microbubbles examined in the present study are characterized by a resonance frequency on the order of 1 MHz and a significant damping rate; hence they achieve saturation quite fast, i.e., after a few periods of the radial pulsation.

The force that accelerates the bubble towards the wall is due to the scattered pressure that is emitted by the wall in response to the original pressure wave from the pulsating bubble [6,10,12,13,32], in the range of validity of potential flow as is the case in the present study. As long as the bubble center of mass remains relatively far from the wall, dimensional distance $z'_c \geqslant 2R_0$, the scattered pressure from the wall can be approximated by potential theory via the scattered pressure field due to an image bubble that is located at twice the distance from the original bubble, z'_c, and pulsates in phase with it [10,32]:

$$P' = \frac{\rho}{r'}\frac{d}{dt'}(\dot{R}'R'^2), \quad \frac{\partial P'}{\partial r'} = -\frac{\rho}{r'^2}\frac{d}{dt'}(\dot{R}'R'^2), \quad r' = 2z'_c. \tag{16}$$

Upon ignoring viscous effects, Re $\gg 1$, the force on the original bubble is provided by the integral of the scattered pressure ($\boldsymbol{n}_B$ points towards the bubble interior and $\boldsymbol{e}_r$ is the radial unit vector originated at the image bubble and directed towards the bubble that approaches the wall):

$$\boldsymbol{F} = \iint_{A'} P'\boldsymbol{n}_B dA' = -\iint_{A'} P'\boldsymbol{n} dA' = -\iiint_{V'} \nabla P' dV' \xrightarrow[r'=2z'_c]{r'\gg R_0}$$

$$\boldsymbol{F} \approx \nabla P' V' = -V'\left.\frac{\partial P'}{\partial r'}\right|_{r'=2z'_c}\boldsymbol{e}_r = \frac{\rho}{4\pi(2z'_c)^2}V'\frac{d^2V'}{dt'^2}\boldsymbol{e}_r, \tag{17}$$

with V' denoting the instantaneous bubble volume. Averaging over a period $T = 2\pi/\omega_f$ of the volume pulsation we recover the secondary Bjerknes force:

$$\boldsymbol{F}_B = \langle \boldsymbol{F} \rangle = -\frac{\rho}{4\pi (2z'_c)^2} \frac{\int_T \dot{V}'^2 dt'}{T} \boldsymbol{e}_r, \quad V' = \frac{4}{3}\pi R'^3(t'), \tag{18}$$

which is responsible for the bubble motion towards the wall. When the bubble is excited by a small amplitude acoustic disturbance in the manner shown in Eq. (11), it eventually settles to the above described saturated pulsation, Eq. (13), with amplitude $\delta_o R_0$ provided by the maximum excursion from equilibrium. The latter is quite small even for large pressure disturbances, and, consequently, by linearizing and taking averages over one period of the steady pulsation we recover the classic expression for the secondary Bjerknes force:

$$R' = R_0 + R'_D(t') \rightarrow \frac{R'_D}{R_0} \approx 1 + \delta_o \cos t, \quad V' = \frac{4\pi R_0^3}{3}(1 + 3\delta_o \cos t),$$
$$\boldsymbol{F}_B = -2\pi \rho {\delta_o}^2 \omega_f^2 R_0^4 \left(\frac{R_0}{2z'_c}\right)^2 \boldsymbol{e}_r, \tag{19}$$

with the minus sign indicating attraction towards the mirror bubble or the wall. Clearly this is a second order effect in terms of the sound amplitude and its impact on the bubble motion becomes evident on a long timescale with respect to the period of the forcing $2\pi/\omega_f$.

III. NUMERICAL METHODOLOGIES

A. Numerical method

A detailed description of the numerical methodology that is used to simulate the dynamic behavior of a contrast agent in an unbounded flow when the viscous forces of the surrounding liquid are accounted for is provided in Vlachomitrou and Pelekasis [23]. In the present study we use the same numerical approach and we extend it in order to take into account wall presence.

As in the case of the unbounded flow, numerical solution is performed via the Galerkin finite element methodology with a hybrid scheme that uses two-dimensional (2D) Lagrangian functions to discretize the surrounding flow field, in conjunction with one-dimensional (1D) cubic splines for the bubble shape. In the case of an encapsulated bubble the introduction of cubic splines is necessary because a fourth order derivative arises in the force balance equation through the bending resistance of the membrane. More specifically, biquadratic and bilinear Lagrangian basis functions are used for the velocity and the pressure of the liquid, respectively, while cubic spline functions are employed to discretize the interface. The fully implicit Euler time integration scheme is introduced in order to make optimal use of its numerical dissipation properties against the growth of short wave instabilities. In this context, the discretized forms of continuity and Navier-Stokes equations are

$$\iiint N_i \nabla \cdot \boldsymbol{u} dV = 0, \tag{20}$$

$$\iiint M_i \frac{\partial \boldsymbol{u}}{\partial t} \cdot \boldsymbol{e_k} dV + \iiint M_i (\boldsymbol{u} \cdot \nabla)\boldsymbol{u} \cdot \boldsymbol{e_k} dV + \iiint M_i \nabla P \cdot \boldsymbol{e_k} dV - \frac{1}{\mathrm{Re}} \iiint M_i \nabla \cdot \underline{\underline{\tau}} \cdot \boldsymbol{e_k} dV = 0, \tag{21}$$

where M_i, N_i are the biquadratic and bilinear Lagrangian functions, respectively; $dV = rdrdzd\theta$ is the differential volume of integration; and vector $\boldsymbol{e_k}$ refers to one of the unit vectors $\boldsymbol{e_r}, \boldsymbol{e_z}$ corresponding to the components of the differential momentum balance. Upon integrating by parts,

Eq. (21), the r and z components of the weak formulation of the momentum equation are derived:

$$\int\int_A \left[M_i \left[\frac{\partial \boldsymbol{u}}{\partial t} + (\boldsymbol{u}\cdot\nabla)\boldsymbol{u} \right] \cdot \boldsymbol{e_k} - P\nabla\cdot(M_i\boldsymbol{e_k}) + \underline{\underline{\boldsymbol{\tau}}} : \nabla(M_i\boldsymbol{e_k}) \right] r dr dz$$
$$+ \oint_\Gamma M_i(-\boldsymbol{n}) \cdot \left(P\underline{\underline{\boldsymbol{I}}}\cdot\boldsymbol{e_k} - \frac{1}{Re}\underline{\underline{\boldsymbol{\tau}}}\cdot\boldsymbol{e_k} \right) r dS = 0. \tag{22}$$

The azimuthal angle θ has been integrated out of the above equations due to axisymmetry, essentially generating a two-dimensional geometry to be discretized with a line integral at its boundary.

The continuity of the radial and axial velocity components is imposed as an essential boundary condition on the interface. Furthermore, since we employ a Lagrangian representation for the shape of the bubble we need two equations for each particle, ξ, to determine the two coordinates $r(\xi,t)$ and $z(\xi,t)$. For this reason the normal and tangential force balances are employed and are discretized using the one-dimensional cubic splines B_i as basis functions:

$$\int B_i \left(-P\underline{\underline{\boldsymbol{I}}} + \frac{1}{\mathrm{Re}}\underline{\underline{\boldsymbol{\tau}}}_l \right) \cdot \boldsymbol{n} dS + \int B_i P_G \boldsymbol{n} dS - \int \frac{1}{\mathrm{We}} B_i 2k_m \boldsymbol{n} dS + \int B_i \boldsymbol{\Delta F} dS = 0, \tag{23}$$

where the integration length is defined as $dS = \sqrt{r_\xi^2 + z_\xi^2}\, d\xi$ in terms of the Lagrangian variable ξ. Finally, on the far field the imposed pressure disturbance is prescribed, while the velocity components are set to zero. In all simulations presented in this paper the far field was considered to be 10 rest radii away from the bubble centroid. In order to ensure the validity of the velocity boundary condition on the outer edge we also performed simulations for larger distances as well that led to the same results.

The nonlinearity of the problem is treated with the Newton-Raphson method and the following linear system of equations is solved during each iteration:

$$\underline{\underline{\boldsymbol{J}}} \cdot d\boldsymbol{C} = \boldsymbol{R}, \tag{24}$$

with $\boldsymbol{R}$ denoting the residual vector, $d\boldsymbol{C}$ the vector of the incremental variation of the unknowns during each iteration, and $\underline{\underline{\boldsymbol{J}}}$ the Jacobian matrix of the system. Vector $d\boldsymbol{C}$ includes the two components of the velocity and the liquid pressure, the gas pressure and the shape of the bubble. The Jacobian matrix $\underline{\underline{\boldsymbol{J}}}$ contains the finite element discretization of the momentum and continuity, Eqs. (19,21), where the fully implicit Euler time integration scheme is implemented, along with the tangential and normal force balances at the interface, Eqs. (23), and the isothermal law for the pressure variation in the bubble, Eq. (10). In this fashion, the Jacobian matrix assumes the form of an arrow with the gas pressure and the bubble shape occupying the arrow columns.

In order to reduce computational time we have chosen to solve the problem iteratively with the GMRES (generalized minimum residual) with right or left preconditioning [33] rather than a direct method. The preconditioning is performed using incomplete lower upper (ILU) factorization. The implementation of ILU and GMRES is performed using SPARSKIT software [34]. It is the experience of the authors that the use of GMRES reduces computational time dramatically and indeed that was seen to be the case in the present study as well. As an extra effort to further reduce computational time we avoid construction and incomplete LU factorization of the Jacobian matrix for every time step. The number of time steps over which the Jacobian matrix can remain unaltered without compromising the efficiency of the algorithm depends strongly on the intensity of the shape deformation of the bubble and was seen to vary considerably between 1 and 500 time steps.

As an overall numerical procedure, at each time step the numerical solution is performed in two stages. In the first stage a Newton-Raphson method is applied in order to solve simultaneously for the velocity and pressure fields along with the shape of the interface. In the second stage, a separate Newton-Raphson iterative procedure follows the above time integration process for the implementation of the elliptic mesh generation scheme and the construction of the updated grid. In

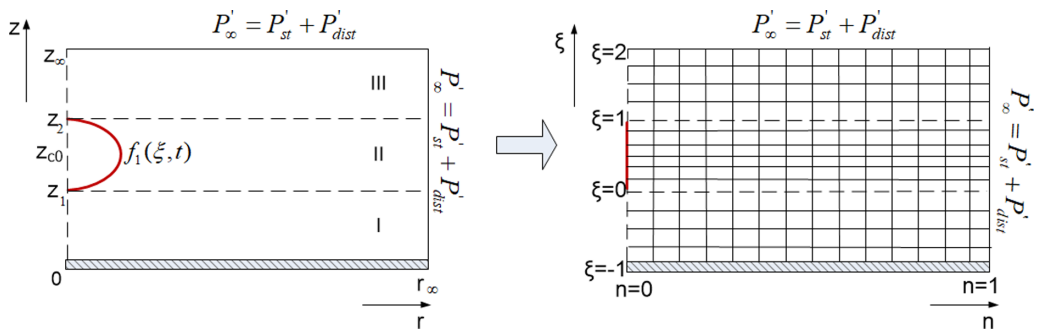

FIG. 2. Schematic representation of the physical and the computational domain for the case of a bubble in wall restricted flow.

the latter stage the shape of the bubble is already known and is imposed as an essential condition for the solution of the elliptic equations that provide the grid coordinates.

B. Grid construction

The elliptic mesh generation technique is employed for the grid construction. In Vlachomitrou and Pelekasis [23] the elliptic transformation was employed, with the boundary conditions that Dimakopoulos and Tsamopoulos [35] proposed, based on the previous work of Christodoulou and Scriven [36] and Tsiveriotis and Brown [37], and appropriate changes were made in order to make it suitable for the simulation of contrast agents in an unbounded flow. More specifically, in the latter studies Lagrangian basis functions are used for the flow as well as for the shape of the interface. The force balance equation is inserted as a natural condition in the flow equations and upon solution of the flow problem the kinematic condition is solved together with the elliptic equations to obtain the shape of the interface and the mesh. However, when coated microbubbles are simulated we introduce a superparametric scheme for the mesh construction that combines the 2D Lagrangian basis functions for the flow field with the 1D cubic splines for the location of the interface [23]. In this fashion discretization of the interfacial force balance equations is facilitated as they contain fourth order derivatives in the form of the bending stresses, with the spline functions interpolating the radial and azimuthal coordinates of the microbubble. At the same time continuity of the radial and azimuthal velocity components is imposed as an essential boundary condition. With this methodology we are able to simultaneously solve for the velocity and pressure fields along with the shape of the interface. Subsequently, the resulting shape is used as an essential condition to construct the mesh. The above procedure offers a significant advantage in that it allows for accurate discretization of the bending stresses and use of greater time steps compared to the original method.

Pertaining to mesh generation in the present study we use the method that was developed in Vlachomitrou and Pelekasis [23], extended in order to take into account wall presence. To this end, we divide the physical domain into three regions: region I is defined as the area between the rigid wall and the lower pole of the bubble, region II includes the area that is defined by the two poles of the bubble, and region III occupies the area between the upper pole and the far field. In this manner we can control the number of elements that is used in each of the three subdomains in the z direction. Thus, in regions I, II, and III we use $N_1 \times M$, $N_2 \times M$, and $N_3 \times M$ elements, respectively, with N_1, N_2, N_3, and M denoting the number of Lagrangian elements used in each one of the above defined subdomains and in the radial direction, respectively. In Fig. 2 a schematic representation of the physical and computational domain that is generated in this fashion is shown.

In this context, we introduce in each region the transformation $(r, z, t) \xrightarrow{J} (\eta, \xi, t)$ with $J = \mathrm{r}_\eta z_\xi - z_\eta \mathrm{r}_\xi$ signifying the Jacobian of the mapping ($0 \leqslant \eta \leqslant 1$ and $-1 \leqslant \xi \leqslant 0$, $0 \leqslant \xi \leqslant 1$, and $1 \leqslant \xi \leqslant 2$ in regions I, II, and III, respectively). Thus, every particle occupying position (r, z) in

a particular time instant is mapped onto a grid point with coordinates (η, ξ). Subsequently, the coordinates of the grid points in the physical domain are defined by solving the following set of partial differential equations [35,37]:

$$\nabla \cdot \left(\varepsilon_1 \sqrt{\frac{r_\xi^2 + z_\xi^2}{r_\eta^2 + z_\eta^2}} + 1 - \varepsilon_1 \right) \nabla \xi = 0, \tag{25}$$

$$\nabla \cdot \nabla \eta = 0. \tag{26}$$

The first equation produces the η curves which must be nearly perpendicular to the interface, whereas the second equation generates the ξ curves which are nearly parallel to the interface and are prescribed so that they follow its deformation. Introduction of the term $\sqrt{\frac{r_\xi^2+z_\xi^2}{r_\eta^2+z_\eta^2}}$ allows the η curves to intersect the interface almost orthogonally, while ε_1 is an empirical parameter that ranges between 0 and 1 and controls the extent of mesh smoothness vs its orthogonality. Its value in each problem is defined by trial and error and in our case is set to 0.1. Upon application of the finite element methodology Eqs. (25) and (26) assume the form

$$\iint \left(\varepsilon_1 \sqrt{\frac{r_\xi^2 + z_\xi^2}{r_\eta^2 + z_\eta^2}} + 1 - \varepsilon_1 \right) \nabla \xi \cdot \nabla M_i dr dz = 0, \tag{27}$$

$$\iint \nabla \eta \cdot \nabla M_i dr dz = 0, \tag{28}$$

where M_i are the biquadratic Lagrangian basis functions. In the above equations the integral terms that the divergence theorem produces are omitted in order to weakly impose orthogonality of the grid lines in the boundaries.

Apart from the elliptic transformation, the appropriate boundary conditions must be introduced. In any boundary where the coordinate is known, the corresponding equation for the grid is not written. Instead, the value of the coordinate is imposed as an essential boundary condition. In the boundaries where we need to control the node distribution the penalty method is applied, as it is necessary to use this condition on the n-grid lines that start from the two poles of the bubble and evolve parallel to the wall; see also Chatzidai *et al.* [38]. In order to apply the penalty method Eq. (27) becomes

$$\iint \left(\varepsilon_1 \sqrt{\frac{r_\xi^2 + z_\xi^2}{r_\eta^2 + z_\eta^2}} + 1 - \varepsilon_1 \right) \nabla \xi \cdot \nabla M_i dr dz + L \int \frac{\partial M_i}{\partial \xi} \sqrt{w_1 r_\xi^2 + w_2 z_\xi^2} ds = 0, \tag{29}$$

where L is a penalty parameter of order $\mathrm{L} = \mathrm{O}(10^3 - 10^5)$ and w_1, w_2 weights that are normally chosen with trial and error. The two weights must satisfy the equality $w_1 + w_2 = 2$ while in the case that $w_1 = w_2 = 1$ the boundary nodes are equally distributed.

A problem that arises when the bubble reaches close to the wall pertains to the fact that the n lines that are parallel to the wall tend to pull away from it, Fig. 3(a). In order to overcome this problem we need to split the entire domain into two different subdomains in the manner shown in Fig. 3(b). In this case, we first construct the grid for the domain between $z = 0$ and $z = 4$ by considering three different regions in this area with the above described procedure. Then we construct the grid in the domain between $z = 4$ and $z = 8$—the latter axial position is treated as the far field—using the values that were calculated from the construction of the first subdomain in line $z = 4$ as essential boundary conditions.

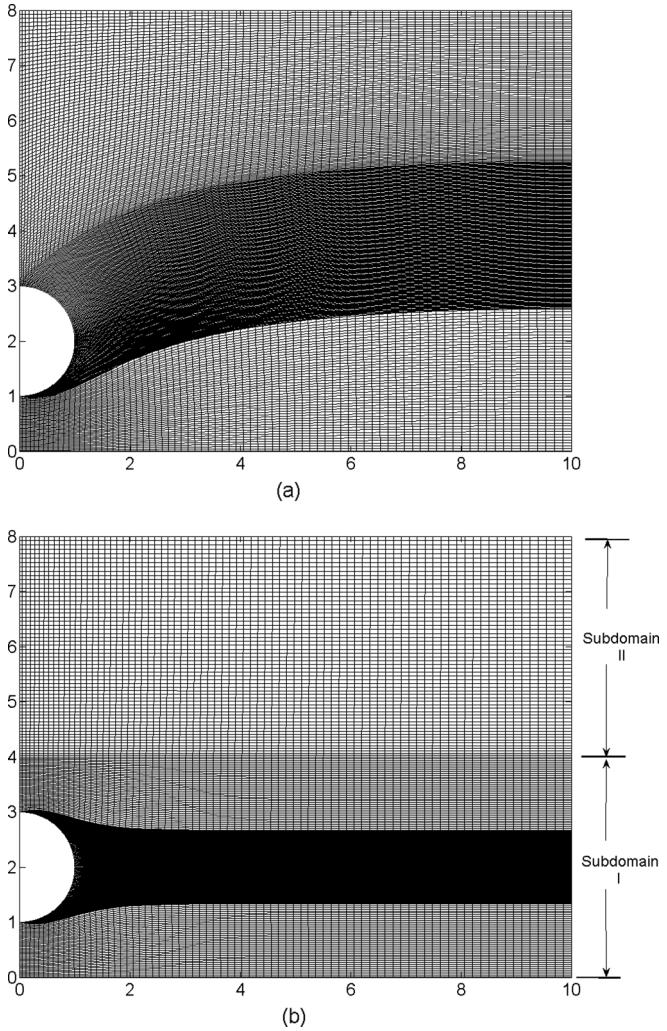

FIG. 3. (a) Construction of the grid in one domain and (b) construction of the grid in two separate subdomains.

C. Benchmark simulations and code validation

In order to validate our methodology, we first consider the case of an encapsulated bubble that is initially placed at a relatively large distance between the initial center of mass of the bubble and the wall, $z_{c0} \to \infty$, see also Fig. 2(a), and thus the response pattern is expected to exhibit mild deviations from the unbounded flow arrangement. The microbubble is coated by a phospholipid shell that is subjected to an acoustic disturbance in the far field. Indicative values pertaining to soft phospholipid shells are employed, that have previously been used for performing dynamic simulations with the boundary element method [19], and have been cross-checked against relevant studies from the literature of contrast agents [26,39]. The bubble is initially of spherical shape with a radius of $R_0 = 3.6\,\mu$m, and the shell is stress free with viscosity $\mu_s = 60 \times 10^{-9}$ kg/s, area dilatation modulus $\chi = 0.24$ N/m, and bending modulus $k_B = 3 \times 10^{-14}$ N m, while obeying the Mooney-Rivlin constitutive law with the degree of softness b set to zero [26,31]. The surface tension σ is set to 0.051 N/m, the polytropic ideal gas constant to $\gamma = 1.07$, the surrounding liquid is

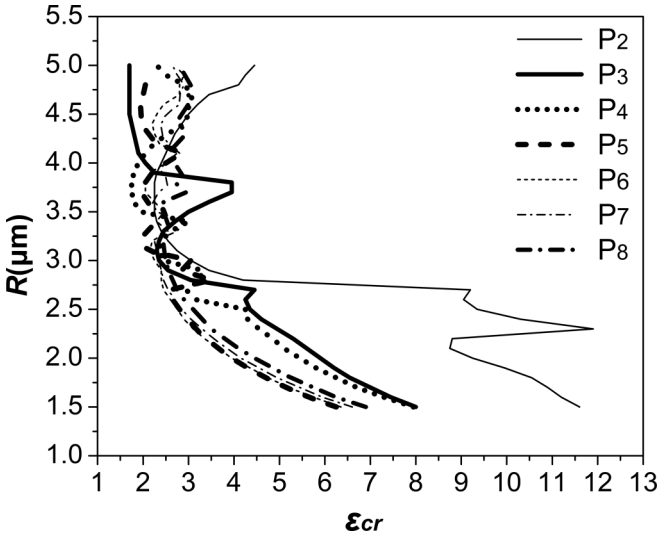

FIG. 4. Phase diagram for a contrast agent with $\mu_s = 60 \times 10^{-9}$ kg/s, $\chi = 0.24$ N/m, and $k_B = 3 \times 10^{-14}$ N m subject to an acoustic disturbance with forcing frequency $f = 1.7$ MHz.

assumed to have the properties of water, and the far field static pressure is taken to be the standard ambient pressure of 1 atm. Tsiglifis and Pelekasis [19] assumed inviscid flow in the surrounding liquid and performed simulations covering a wide parameter range for this particular bubble, using the boundary element method. They used an acoustic disturbance of frequency 1.7 MHz and two different amplitudes, namely, $\varepsilon = 2$ and $\varepsilon = 4$. For both amplitudes they reported shape modes. In particular, for the case with amplitude $\varepsilon = 2$—which, according to stability analysis [21] as illustrated in the phase diagram of Fig. 4, is slightly greater than the critical value ε_{cr}, for the onset of parametric instability—they observed steady shape oscillations in harmonic resonance. It was thus seen that shape modes obtain their maximum amplitude when the volume of the bubble becomes minimum and that they oscillate at approximately the same period with the volume pulsation which is determined by the external forcing. The fourth Legendre mode (P_4) is indicated as the dominant shape mode in the dynamic response of the microbubble, as the sound amplitude increases (Fig. 4); Legendre polynomials arise as the shape eigenfunctions along the azimuthal θ direction for a freely pulsating conventional or coated microbubble [12,21]. In this context, Table I provides the amplitude thresholds for shape mode excitation for the parameter range investigated in the present study. When the sound amplitude was further increased ($\varepsilon = 4$) dynamic buckling was reported [21], also in accordance with the phase diagram provided in Fig. 4. The latter effect takes place in an explosive manner at quite large amplitudes, when the surface acceleration increases significantly during the rebound phase of the volume pulsation, in a manner that is similar to the Rayleigh-Taylor

TABLE I. Amplitude thresholds, $\boldsymbol{\varepsilon}_{cr}$, for parametric mode excitation as a function of the shell viscoelastic properties and sound amplitude. The microbubble stress free radius is set to $R_0 = 3.6\,\mu$m, the bending resistance to $k_B = 3 \times 10^{-14}$ N m, and the Poisson ratio to 0.5. Bold ε's indicate critical thresholds.

χ (N/m)	k_B (N m)	μ_s (kg/s)	f (MHz)	$\boldsymbol{\varepsilon}_{\rm cr}(P_2)$	$\boldsymbol{\varepsilon}_{\rm cr}(P_3)$	$\boldsymbol{\varepsilon}_{\rm cr}(P_4)$	$\boldsymbol{\varepsilon}_{\rm cr}(P_5)$	$\boldsymbol{\varepsilon}_{\rm cr}(P_6)$	$\boldsymbol{\varepsilon}_{\rm cr}(P_7)$	$\boldsymbol{\varepsilon}_{\rm cr}(P_8)$
0.12	3×10^{-14}	120×10^{-9}	1.7	6.6	5	4.5	3.5	2.95	2.6	**2.55**
0.24	3×10^{-14}	60×10^{-9}	1.7	2.2	3.4	**1.75**	2.05	2.25	2.2	2.45
0.24	3×10^{-14}	120×10^{-9}	1.7	5.45	4.75	4.3	3.45	2.85	**2.5**	**2.5**
0.48	3×10^{-14}	120×10^{-9}	1.7	4.65	4.1	3.85	3.15	3.3	**2.25**	**2.25**

instability of free surfaces. With the present methodology that fully accounts for liquid viscosity and incorporates the interaction with a nearby rigid wall the above effects are recovered and enriched due to the interaction. For very large initial dimensionless distance between the microbubble and the wall, $z_{c0} = \frac{z'_{c0}}{R_0} = \frac{z'_c(t'=0)}{R_0}$, its response as it pulsates in free space is recovered with a mild modification owing to the impact of liquid viscosity. In particular, harmonic mode excitation is captured albeit after a longer time period which highlights the stabilizing role of liquid viscosity in delaying the onset of shape deformation. In fact, shape pulsations of appreciable magnitude were observed after an inception phase on the order of 40 periods, at sound amplitude as large as $\varepsilon \sim 2.5$. Harmonic shape excitation occurs at smaller amplitudes as well; however, it takes much longer to evolve to a significant level. Figure 5 provides the numerical results obtained with the present methodology, in terms of the shape and mode evolution, for a coated microbubble with the above properties that freely pulsates away from boundaries, subject to an acoustic disturbance. The interfacial shape is illustrated in terms of the Cartesian coordinates $z_B = r_{\text{sph}} \cos\theta$ and $x = r_{\text{sph}} \sin\theta$ where $r_{\text{sph}}, \theta, \varphi$, signify spherical coordinates with θ, φ denoting the azimuthal and polar angles. In this context the (x, z_B) plane is obtained by joining the $\varphi = 0$ and π coordinate surfaces, while the z_B coordinate is aligned with the axis of symmetry with its origin located at the geometric center of the bubble. Axial coordinate z, used in the graphs illustrating the bubble shape as it interacts with the wall, is translated so that its origin lies at the wall. For an axisymmetric shape the interface has to be symmetric in the (x, z_B) plane with respect to the z_B axis. We have used 200 elements on the membrane and 80 elements for the flow, in the manner described by Vlachomitrou and Pelekasis [23] whereas the time step was set to 0.01.

As is clearly illustrated in Figs. 5(a) and 5(c) obtained when $\varepsilon = 2.5$, as time evolves steady shape oscillations are established in harmonic resonance with the forcing, that are dominated by the fourth Legendre mode P_4, in accordance with stability analysis, followed in intensity by P_6 and P_8. Consequently, the bubble eventually exhibits steady pulsations with a shape that is characterized by four lobes during compression, whereas it eventually becomes almost spherical during the expansion phase, Fig. 5(a). When the sound amplitude is raised to 3, steady pulsations are not observed. Rather the microbubble is destabilized in a similar fashion with the simulations performed by Tsiglifis and Pelekasis [19]. As illustrated in Figs. 5(b) and 5(d) rapid growth of higher shape modes, predominantly P_8, is obtained in the rebound phase of the pulsation following the onset of minimum bubble volume. This takes place after a longer time period in comparison with the boundary element simulations by Tsiglifis and Pelekasis, due to the impact of liquid viscosity, but is overall characterized by the same dynamic pattern identified as dynamic buckling [19,21].

In order to stress the effect of the wall on the microbubble response, as well as to verify that the results are grid independent, the simulations were repeated with the microbubble center of mass initially located at a dimensionless distance $z_{c0} = 6$ from the wall. It should be stressed that even at this relatively large distance the wall effect is evident. In fact repeating the simulation shown in Fig. 5 with z_{c0} set to the above value, while keeping the rest of the problem parameters the same, accelerates the onset of dynamic buckling instability by halving the time required for significant shell deformation to take place without, however, altering the dominant shape modes. Thus, the microbubble soon loses coherence before reaching the wall. Consequently, the simulation was repeated with a lower sound amplitude and Fig. 6 presents the dynamic response of the microbubble that was interrogated in Fig. 5 for an initial distance from the wall of $z_{c0} = 6$ and a sound amplitude of $\varepsilon = 2$. The shape of the interface in Fig. 6 is illustrated in terms of the axial cylindrical coordinate z that practically expresses the distance of each interfacial particle from the wall and the Cartesian coordinate $x = r_{\text{sph}} \sin\theta$. Two different mesh sizes were employed and compared. In the first grid, G_1, [Figs. 6(a) and 6(b)] we used 50, 100, and 50 elements in regions I, II, and III of the z direction, respectively, and 60 elements in the r direction [see Fig. 2(a)]. A denser grid, G_2, was also employed [Figs. 6(c) and 6(d)] with 100, 200, and 100 elements in the three regions of the z direction, respectively, and 80 elements along the r direction. Although the discussion and the interpretation of the results presented in Fig. 6 are left for the next section, it is obvious that there

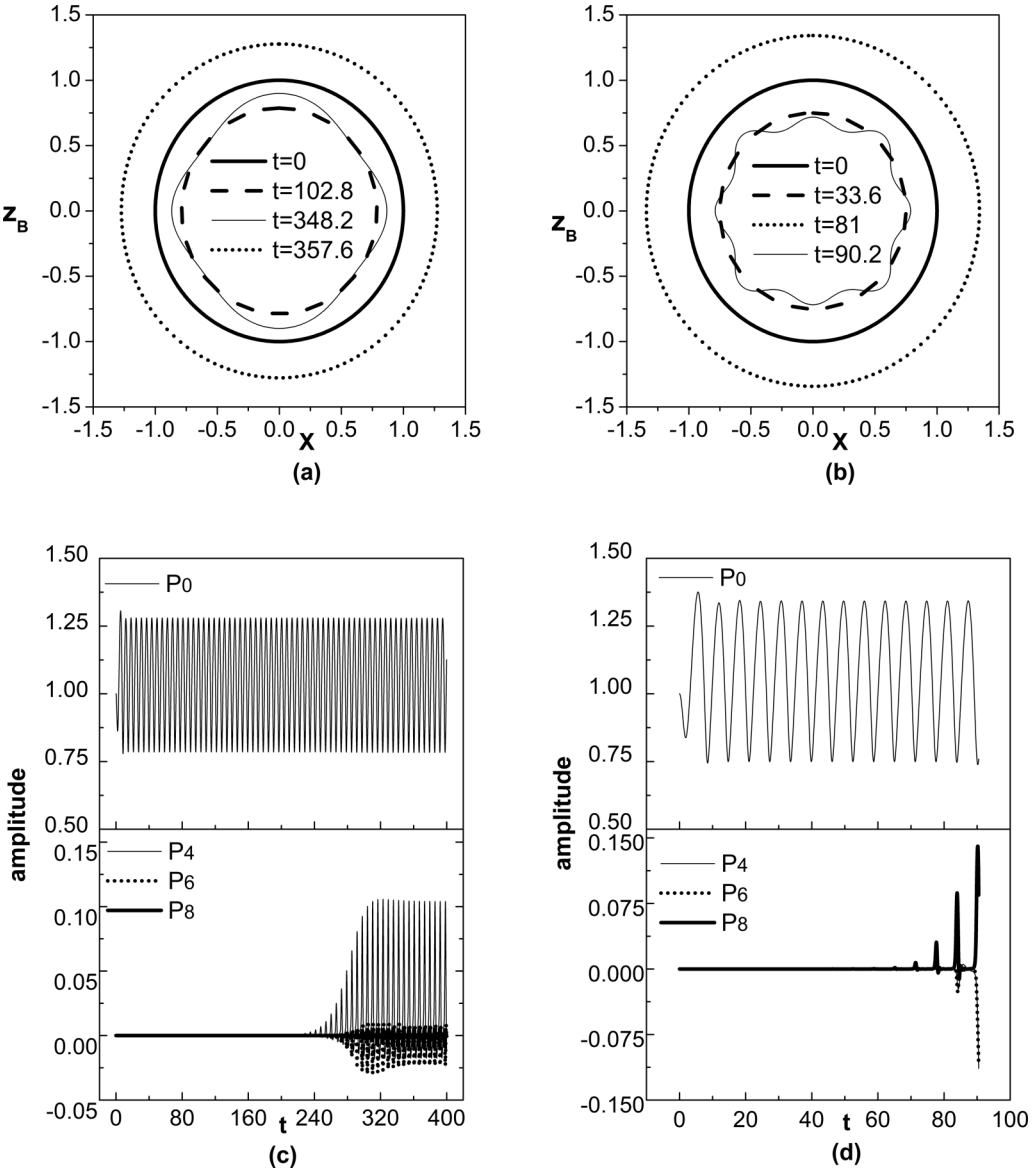

FIG. 5. Temporal evolution of (a), (b) bubble shape and (c), (d) breathing, P_0, and shape mode, P_4, P_6, P_8, decomposition for a contrast agent with $R_0 = 3.6\,\mu$m, $\mu_s = 60 \times 10^{-9}$ kg/s, $\chi = 0.24$ N/m, and $k_B = 3 \times 10^{-14}$ N m that freely pulsates away from nearby surfaces, subject to an acoustic disturbance with forcing frequency $f = 1.7$ MHz and sound amplitude $\varepsilon = 2.5$ and 3, respectively.

is sufficient numerical convergence and both meshes are able to capture successfully the motion of the microbubble towards the wall, as well as the interfacial distortions. The superiority of the denser grid is mostly illustrated in the snapshot of $t = 52.6$, Fig. 6(c), since the sparse grid, Fig. 6(a), is unable to capture bending in the area near the north pole.

Even though the numerical results presented in Fig. 6 have already achieved convergence, we chose to use dense grids in all simulations of this study to ensure higher accuracy despite the increase in computational cost. Thus, in all simulations of Sec. IV we used 80–100, 200, and

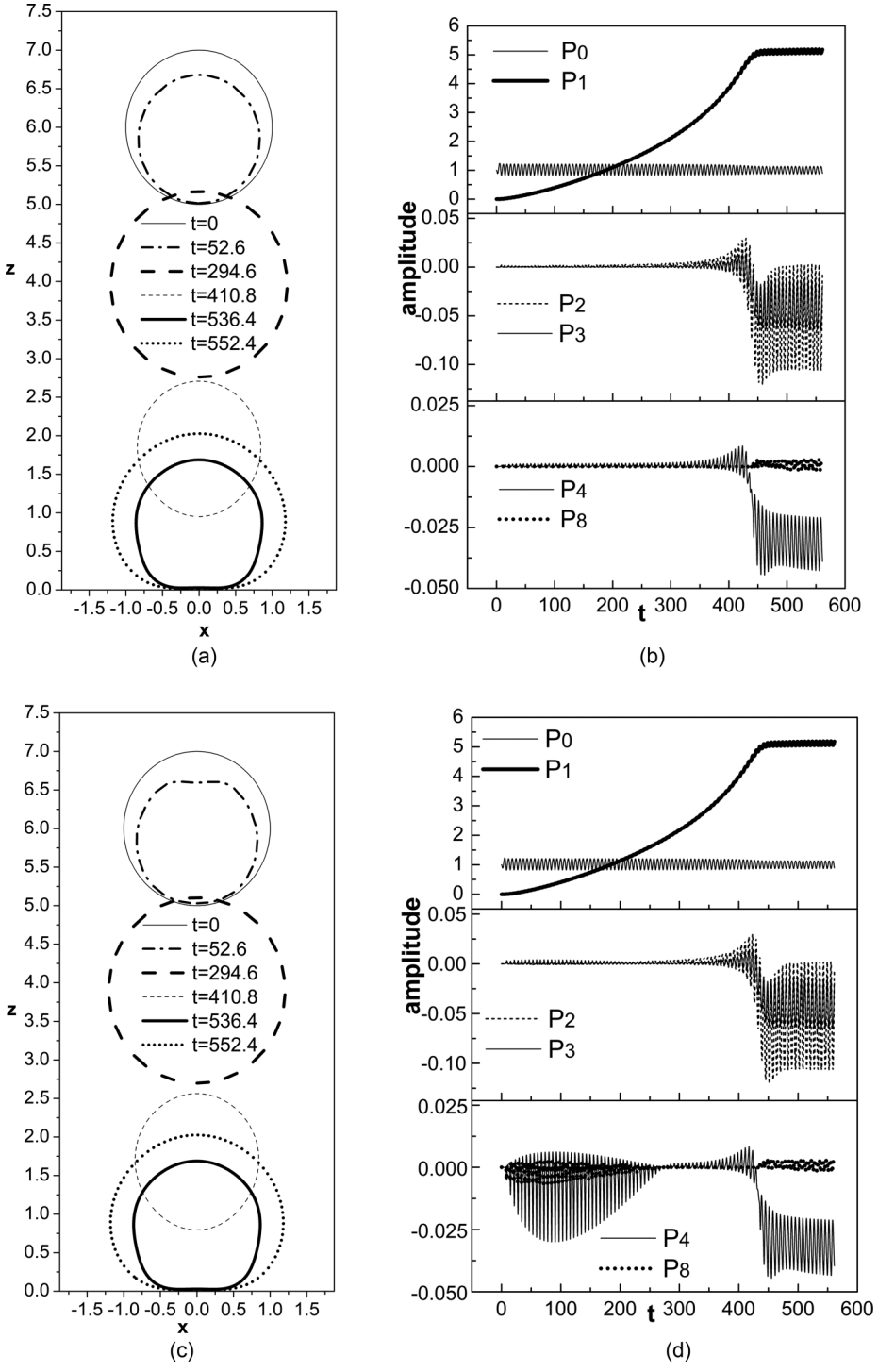

FIG. 6. Temporal evolution of (a), (c) bubble shape and (b), (d) breathing, P_0, translational P_1 modes, and shape mode decomposition for grids G_1 and G_2, respectively; the initial bubble radius is $R_0 = 3.6\,\mu$m; shell properties are $\mu_s = 60 \times 10^{-9}$ kg/s, $\chi = 0.24$ N/m, and $k_B = 3 \times 10^{-14}$ N m; the initial distance from the wall is set to $z_{c0} = 6$; an acoustic disturbance of frequency $f = 1.7$ MHz and sound amplitude $\varepsilon = 2$ are imposed.

80–100 elements in regions I, II, and III of the z direction, respectively, whereas 80–120 elements were employed in the r direction. At this point it is important to mention that an advantage of the employed method is that the number of elements occupied in each subregion of the domain remains constant throughout the simulation. This means that as the bubble moves closer to the wall the grid becomes denser in the area between the bubble and the wall where higher accuracy is most needed. Finally, the time step was set to 0.01 in all simulations, although smaller time steps (up to 0.001) were also tested to ensure sufficient accuracy. As the timescale of the problem is dictated by the external frequency, the nondimensional period of the oscillations is equal to 2π, and consequently $t/(2\pi)$ is a measure of the number of periods that have elapsed during the dimensionless time interval t. In this context, the selected time step is quite small since 628 time steps are employed during one bubble oscillation when a time step of 0.01 is used.

IV. RESULTS AND DISCUSSION

Regarding the motion of the microbbuble, the secondary Bjerknes force accelerates the microbubble towards the wall with a simultaneous radial, $\mathrm{Re} \equiv \rho\omega_f R_0^2/\mu \approx 140$, in the simulations shown in Fig. 6, and translational pulsation. Due to the large shell viscosity transients are soon damped and a saturated pulsation is achieved at the forcing frequency. Since the forcing frequency ω_f is used as the characteristic timescale $t/(2\pi)$ represents the number of imposed sound field periods. Furthermore, due to the incompressibility of the surrounding liquid the time delay between the radial and translational motion is negligible, at least for relatively small amplitudes, as illustrated by the time evolution of P_0 and P_1 shown in Fig. 6(d). Consequently, the latter mode evolves in an oscillatory fashion in phase with volume pulsations and its amplitude is related to the instantaneous center of mass via $a_{P_1}(t) = z_{c0} - z_c(t)$. In this fashion, the speed of approach is gradually increased with time and, provided the acceleration due to the added mass effect is subdominant, it is determined by the instantaneous balance between the Bjerknes force and the viscous drag from the surrounding liquid [10,32]. To test this hypothesis we perform various simulations and we calculate the evolution of the average velocity U of the center of mass during a period of the radial pulsation until the bubble has reached a distance from the wall that is on the order of $z_c' = 2R_0$. Thus, we also evaluate the evolution of the translational Reynolds, $\mathrm{Re}_T \equiv \frac{\rho U 2R_0}{\mu}$, as the bubble approaches the wall for a parameter range pertaining to the shell and acoustic disturbance properties employed in the present study. In particular, we have used the shell parameters shown in Table I and we have considered various liquid viscosities that range between 0.0005 and 0.005 Pa s.

A. Mechanical equilibrium far from the wall

The case shown in Fig. 6 exhibits the parametric mode excitation with P_4 being initially dominant as its excitation threshold is below $\varepsilon = 2$, Fig. 4. It should be stressed, however, that the rigid wall, for a dimensionless initial distance $z_{c0} < 10$, facilitates growth of shape modes within a shorter time interval, in comparison with the freely pulsating bubble simulated in Fig. 5 which had to be perturbed with an amplitude of $\varepsilon \geqslant 2.5$ in order to exhibit a significant deformation from the initial spherical shape on a timescale that is not prohibitively large in terms of CPU time. Thus—and parallel to the pattern of parametric destabilization, i.e., the onset of P_4–P_7 due to parametric excitation—wall proximity instigates bubble deformation represented by the gradual growth of P_2 and P_3 as the distance from the wall decreases, due to the Bjerknes bubble-wall interaction. The concurrent growth of shape modes allows for energy transfer between them and this can be inferred by the envelope in the pulsation of the shape modes in Fig. 6(d). P_2 is the major recipient of this interaction and this is registered in the increasingly prolate shape of the bubble, Fig. 6(c), before the bubble reaches the wall. This behavior is better illustrated in Fig. 7(a) which focuses on the phase of acceleration far from the wall and provides a zoom-in on the evolution of the different shape modes. In particular, when the microbubble pulsates relatively far from the wall higher shape modes, P_4, P_5 etc., appear first during the compression phase of the volume pulsation due to parametric instability,

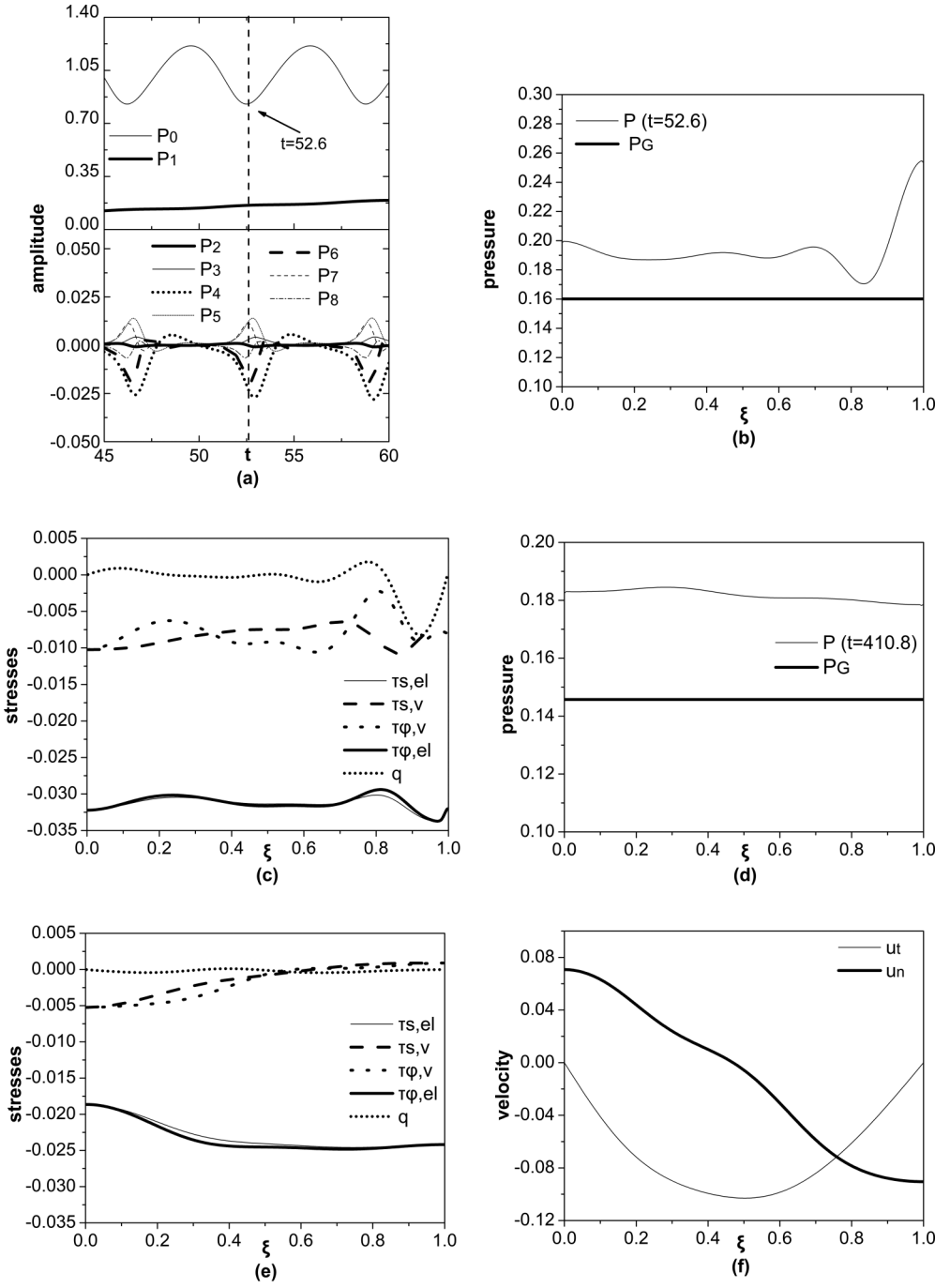

FIG. 7. (a) Zoom-in on the shape mode evolution during the acceleration phase of the pulsation; distribution of (b,d) pressure and (c,e) viscoelastic stresses, at maximum compression during the acceleration phase when $t = 52.6$ and 410.8, respectively; (f) tangential u_t and normal u_n velocities of the liquid when $t = 410.8$; the initial bubble radius is $R_0 = 3.6\,\mu$m; shell properties are $\mu_s = 60 \times 10^{-9}$ kg/s, $\chi = 0.24$ N/m, and $k_B = 3 \times 10^{-14}$ N m; the initial distance from the wall is set to $z_{c0} = 6$; an acoustic disturbance of frequency $f = 1.7$ MHz and sound amplitude $\varepsilon = 2$ are imposed.

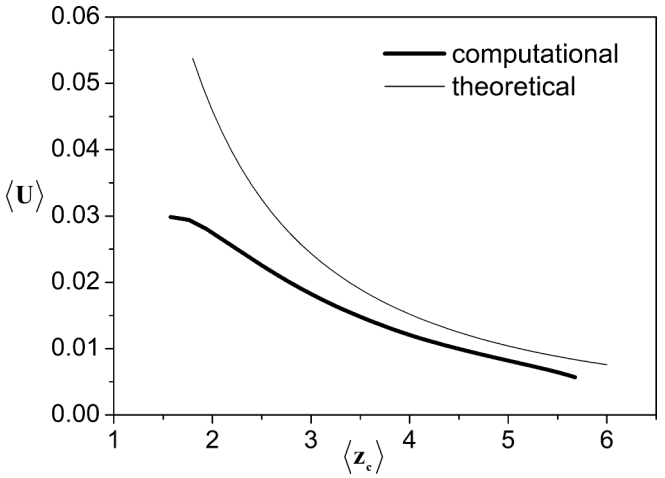

FIG. 8. Comparison of the evolution of the dimensionless translational bubble velocity as a function of distance from the wall calculated numerically and theoretically; the initial bubble radius is $R_0 = 3.6\,\mu$m; shell properties are $\mu_s = 60 \times 10^{-9}$ kg/s, $\chi = 0.24$ N/m, and $k_B = 3 \times 10^{-14}$ N m; the initial distance from the wall is set to $z_{c0} = 6$; an acoustic disturbance of forcing frequency $f = 1.7$ MHz and sound amplitude $\varepsilon = 2$ are imposed.

whereas the bubble remains mostly spherical during expansion. P_2 and P_3 also grow during the compression phase, since this is when translation of the bubble center of mass mostly takes place due to the reduced added mass of the bubble and, consequently, wall interaction is intensified. The above response pattern is halted as the bubble reaches the wall, in the sense that the translational motion is intensely decelerated until the bubble performs trapped pulsations while the shape of its interface reverts from prolate to oblate shapes, Fig. 6(c).

During the acceleration phase the shape is dominated by P_2, with positive amplitude corresponding to a prolate shape, and P_4, and this is manifested in the shapes that are exhibited, Fig. 6(c), as well as in the mode decomposition Figs. 6(d) and 7(a), of the bubble shape as it evolves during its motion towards the wall. During compression the microbubble shell is subject to a larger liquid overpressure, Fig. 7(b), in the region around the pole that faces away from the wall, which results in local compression; see snapshots of the shape for $t = 52.6$ in Fig. 6(c). Furthermore, as illustrated in Fig. 7(c), which shows the distribution of elastic stresses along the bubble interface at $t = 52.6$, the onset of compressive viscous elastic stresses near the north pole ($\xi = 1$) where the maximum overpressure occurs, Fig. 7(b), mitigates the intensity of elastic strain and bending required to establish mechanical equilibrium in that region and prevents jet formation.

As the microbubble accelerates towards the wall the region of maximum overpressure during volume compression is displaced towards the south pole region ($\xi = 0$), Fig. 7(d), and, as will be seen in the following discussion, a balance between radiation pressure and viscous drag is established that is manifested in the evolution of the translational velocity, Fig. 8, as a function of the position of the center of mass with respect to the wall, both averaged over a period of the pulsation $\langle U \rangle$, $\langle z_c \rangle$ in the manner used in Eq. (18) for the definition of Bjerknes force. Consequently, the normal force balance imposes the onset of viscous compressive stresses, mainly in the south pole region where deceleration is more intense, as a means to attenuate compressive elastic stresses that naturally develop as a result of the liquid overpressure. Figures 7(d)–7(f) illustrate this tendency at the instant of maximum compression for which the microbubble clearly acquires a prolate shape, as indicated by the shape obtained at dimensionless time $t = 410.6$ in Fig. 6(c) and by the evolution of the second Legendre mode P_2 which remains positive during this phase of the oscillation; see also Figs. 6(d) and 7(a). In the two pole regions where the normal velocity is higher, Fig. 7(f), this is

sufficient to establish the local normal force balance in the absence of significant bending. However, at the equator where the tangential shell velocity is maximized, Fig. 7(f), and the viscous shell stresses decrease, Fig. 7(e), intense elastic strain develops in order to balance liquid overpressure in the normal force balance while viscous shear from the surrounding fluid balances shell viscous stresses via the tangential stress balance. This pattern dominates shell equilibrium during maximum compression and favors the onset of prolate shapes.

The progressively more intense prolate shape during maximum compression as the bubble approaches the wall, and therefore as the translational velocity increases, is better illustrated in Fig. 9. The three snapshots, Fig. 9(a), belong to the simulation shown in Fig. 6 but are captured at different time instants corresponding to maximum compression and smaller distances from the wall. Clearly as the bubble accelerates towards the wall and Re_T increases tangential viscous stresses from the surrounding liquid become more intense, Fig. 9(d), and establish a balance with shell viscous stresses in the bulk of the shell, in the manner prescribed by the tangential force balance in the absence of significant bending stresses. On the other hand elastic strain is progressively maximized in the equatorial portion of the shell, Figs. 9(b) and 9(c), in order to balance liquid overpressure via the normal force balance. In fact, it was seen that viscous shear from the surrounding liquid balances tangential viscous shell stresses except for the region in the vicinity of the south pole where the development of normal viscous shell stresses, Figs. 9(b) and 9(c), relaxes the intensity of elastic strain required to counteract liquid overpressure. This results in lower compression in comparison with the equator region and consequently enhances the onset of more prolate shapes.

An important aspect of the translational motion of the microbubble towards the wall pertains to the instantaneous balance that is established between the secondary Bjerknes force, F_B, and the viscous drag, F_D, as illustrated in Fig. 9(e) where their time evolution is presented averaged over a period of the volume pulsation. The time evolution of the absolute value, $|F_B|$, is portrayed in Fig. 9(e), of the otherwise negative Bjerknes force since it acts on the opposite direction with respect to viscous drag, along with the integral of the viscous drag on the shell-liquid interface. In the simulation depicted in Fig. 6 the fact that these two opposing forces balance each other is manifested in the form of a nearly constant average acceleration that results in a quadratic dependence of the average distance of its center of mass from the wall as time evolves. To further illustrate this balance, Fig. 8 provides a plot of the variation of the bubble translational velocity as a function of the instantaneous distance from the wall, both averaged over a period of the volume pulsation, obtained numerically through the variation of the center of mass with time shown in Fig. 6(d), and theoretically by implementing the time averaged force balance between Bjerknes force equation (18), and the viscous drag on the bubble via the drag coefficient c_D:

$$F_B = 2\pi\rho{\delta_o}^2\omega_f^2 R_0^4\left(\frac{R_0}{2\langle z'_c\rangle}\right)^2 = F_D = \frac{c_D}{2}\rho\langle U'\rangle^2\pi R_0^2. \tag{30}$$

In this fashion we juxtapose in the $\langle U\rangle$ vs $\langle z_c\rangle$ plane, as illustrated in Fig. 8, the numerically obtained cloud of points and the theoretical curve produced by introducing correlation Eq. 1(c) in the force balance equation (30). Equation 1(c) constitutes a correction to the Stokes law for a translating and pulsating solid sphere. The amplitude $\delta_o \approx 0.18$ of radial pulsation used in Eq. (30) is obtained from the amplitude of P_0 shown in Fig. 6(d). It is in agreement with the value obtained from the linearized Eq. (13) that provides a zoom-in on the mode decomposition in the time period before the bubble reaches the wall. It should be stressed that the balance in Eq. (30) holds provided the translational Reynolds, Re_T, remains an order 1 or larger quantity, in which case the history force is negligible and Eq. 1(c) is valid [17]. It will be seen that this is indeed the case in the present study, hence we adopt the above approach for the estimation of the average bubble translational velocity. The combined theoretical force balance

$$F_B = 2\pi\rho{\delta_o}^2\omega_f^2 R_0^4\left(\frac{R_0}{2\langle z'_c\rangle}\right)^2 = F_D = \frac{c_D}{2}\rho\langle U'\rangle^2\pi R_0^2 = \frac{24}{\mathrm{Re}_T}\left(1+0.15\mathrm{Re}_T^{0.687}\right)\frac{\rho\langle U'\rangle^2\pi R_0^2}{2},$$
$$\mathrm{Re}_T = \frac{\rho\langle U'\rangle 2R_0}{\mu}, \tag{31}$$

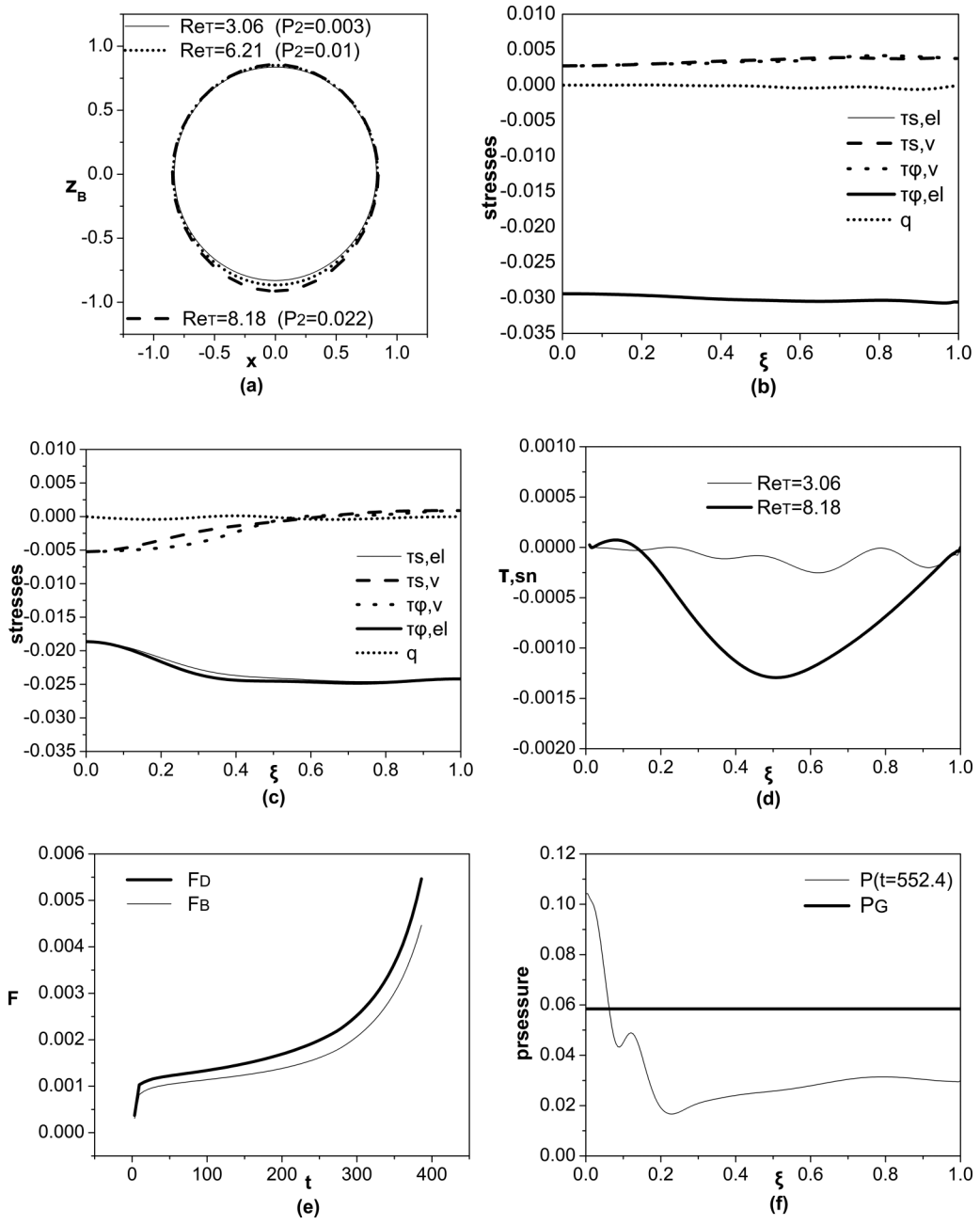

FIG. 9. (a) Prolate shapes during maximum compression for different Re_T; (b), (c) viscoelastic stresses when $\mathrm{Re}_T = 3.06$ and $\mathrm{Re}_T = 8.18$, respectively; (d) liquid tangential stresses when $\mathrm{Re}_T = 3.06$ and $\mathrm{Re}_T = 8.18$, respectively; (e) temporal evolution of the viscous drag force and the absolute value of the secondary Bjerknes force, both obtained numerically; and (f) interfacial distribution of pressure during trapped pulsations: the initial bubble radius is $R_0 = 3.6\,\mu$m; shell properties are $\mu_s = 60 \times 10^{-9}$ kg/s, $\chi = 0.24$ N/m, and $k_B = 3 \times 10^{-14}$ N m; the initial distance from the wall is set to $z_{c0} = 6$; an acoustic disturbance of frequency $f = 1.7$ MHz and sound amplitude $\varepsilon = 2$ are imposed.

incorporates the inverse square dependence with wall distance of the Bjerknes force as the bubble approaches the wall. The two curves agree very well until the dimensionless wall distance $z_c \approx 2$, whereas strong deviations are observed for the late stages of the motion during which the bubble has approached the wall within a distance $z_c' = R_0$, in which case trapped pulsations take place. It should also be stressed that, as illustrated by Fig. 8, as Re_T increases the $\mathrm{Re}_T^{0.687}$ correction to the Stokes law in Eq. (31) increases and tends to produce an inverse linear response pattern, $\langle U' \rangle \sim 1/\langle z_c' \rangle$, from the early stages of the motion. Furthermore, for the parameter range examined in the present study, the initial distance from the wall does not affect the Bjerknes force as the bubble approaches the wall since the bubble achieves almost instantaneously a balance between Bjerknes force and the viscous drag. Consequently, as the process of bubble trapping commences the secondary Bjerknes force at a certain distance z_c does not depend significantly on the initial distance z_{c0}.

The above described response pattern with the acceleration of the center of mass conforming with the findings of potential flow analysis and Bjerknes theory [6,10,12,21,32] does not persist as the microbubble approaches the wall significantly, $z_c' \sim R_0$, in which case lubrication forces emerge in the pole region that faces the wall and significant deviations from sphericity arise in the bubble shape. Growth of lubrication pressure in the south pole region takes the place of viscous shear in counteracting the secondary Bjerknes forces during the late stages of its motion, when trapping by the wall and the onset of steady pulsations take place along with significant shape deformation; see also Fig. 6(c) portraying the evolution of the bubble shape as it performs steady pulsations. Pressure drag, Fig. 9(f), takes the place of viscous drag in counteracting Bjerknes forces and decelerating the bubble motion and this generates oblate shapes instead of the prolate shapes obtained in the bubble acceleration phase.

B. Parametric study

The simulation depicted in Figs. 6–9 is next repeated for an even smaller initial distance from the wall and the same properties of the acoustic excitation, i.e., $\varepsilon = 2\omega_f = 2\pi\, 1.7\,\mathrm{MHz}$ and $z_{c0} = 4$. Figures 10(a) and 10(b) depict the results of the simulations in terms of the evolution of the bubble shape and its mode decomposition. The microbubble exhibits the same pattern of initial acceleration due to the secondary Bjerknes forces until it reaches the rigid boundary in which case it performs trapped pulsations. It should be stressed, however, that in this case growth of higher modes has been suppressed during bubble acceleration, due to simultaneous growth of P_2 and P_3 in the compressive phase of the pulsation that controls bubble translation and deformation as well. This also bears an effect on the microbubble prolate shape that is more pronounced for a smaller initial distance from the wall as can be gleaned by the evolution of bubble shapes, Fig. 10(a) vs Fig. 6(c), and the larger positive P_2 amplitude in the mode decomposition graph, Fig. 10(b) vs Fig. 6(d), due to energy transfer between the parametrically excited shape modes and P_2, P_3 that emerge due to wall interaction. On the other hand, the overall bubble shape and speed during trapping, Figs. 10(a) and 10(c), are very similar to the ones obtained for a larger initial distance z_{c0} from the wall, Figs. 6(c) and 8, signifying the same order of magnitude of the secondary Bjerknes force and the resulting deformation for the same instantaneous distance from the wall. This is in accord with Fig. 8 where the velocity of the center of mass is seen to depend on the inverse distance from the wall as a result of the balance between viscous drag and Bjerknes force for the same instantaneous distance, $z_c(t) \leqslant 14$, between the center of mass and the wall. The $1/\langle z'_c \rangle$ dependence is not evident in Fig. 10(c) since the simulation covers a relatively narrow range of distances while starting at a smaller distance from the wall. Overall, the bubble speed and force at the onset of trapping do not depend on the initial distance, for fixed shell and sound properties, as it was expected based on the analysis presented earlier in this section. It should also be stressed that in both cases, $z_{c0} = 6$ and $z_{c0} = 4$, the bubble is finally trapped on the same distance from the wall and exhibits the same contact length in the near wall region. This is also manifested in the evolution and magnitude of the primary shape modes in Fig. 10(b), P_0, P_1, P_2, and P_3, that exhibit the same pattern as in Fig. 6(d) with the exception that the

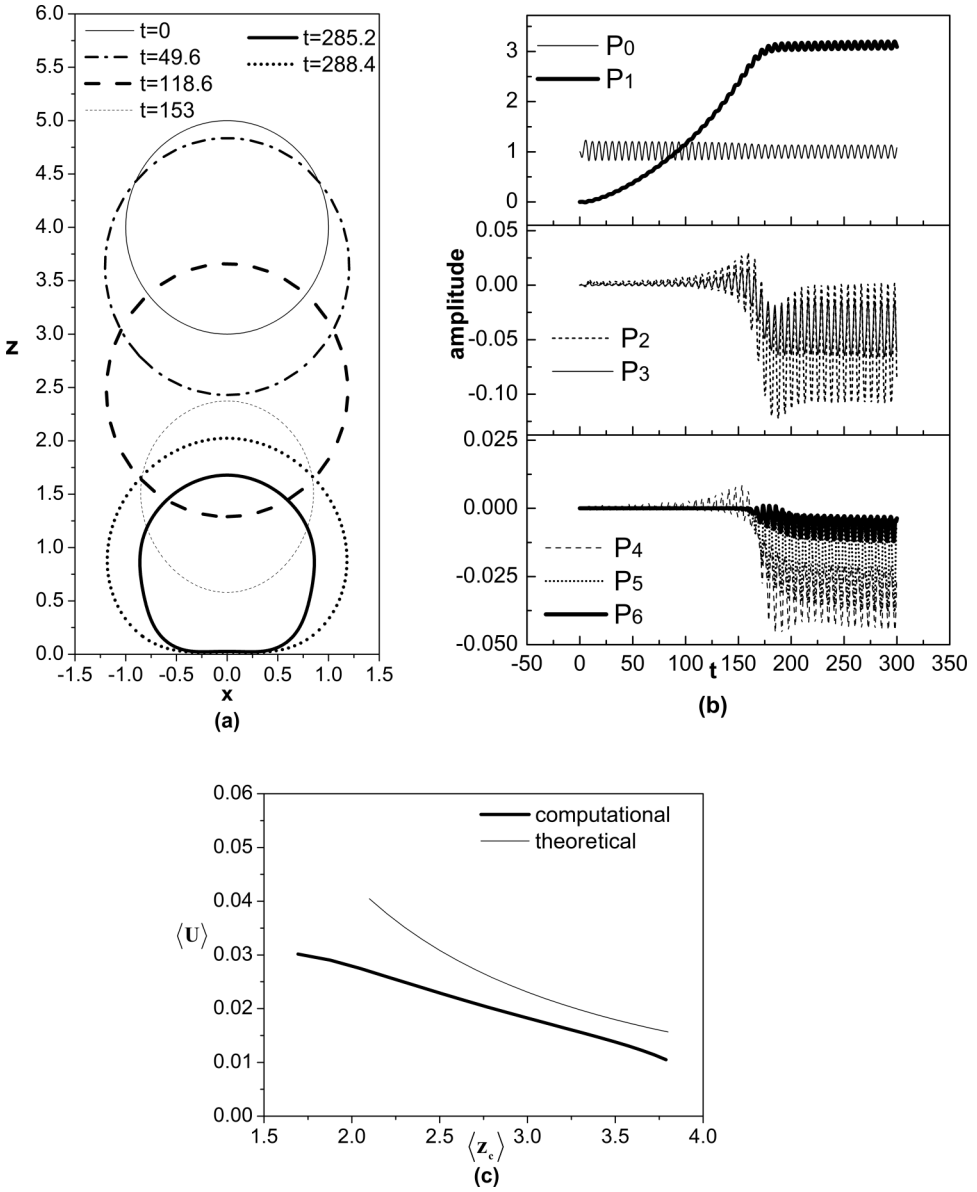

FIG. 10. Temporal evolution of (a) bubble shape; (b) breathing, P_0; translational P_1 modes; and shape mode decomposition; (c) comparison of the evolution of the dimensionless translational bubble velocity as a function of distance from the wall calculated numerically and theoretically: the initial bubble radius is $R_0 = 3.6\,\mu$m; shell properties are $\mu_s = 60 \times 10^{-9}$ kg/s, $\chi = 0.24$ N/m, and $k_B = 3 \times 10^{-14}$ N m; the initial distance from the wall is set to $z_{c0} = 4$; an acoustic disturbance of frequency $f = 1.7$ MHz and sound amplitude $\varepsilon = 2$ are imposed.

bubble reaches the wall, i.e., reaches within one bubble radius from the wall, within a time frame $t \sim z_{c0}^2$.

In this context, the effect that the wall proximity has on the resonance frequency of the microbubble was further examined. Setting the sound amplitude to a relatively low value, well below the threshold for harmonic mode excitation, e.g., $\varepsilon = 0.5$, and the initial distance to $z_{c0} = 6$ while

varying the forcing frequency, the resonance frequency is recovered by registering the maximal radial excursion during expansion over a timescale that is much shorter than the one required for the bubble to reach the wall and trapping to take place. In this fashion a small reduction in the resonance frequency is recovered, $f_0 \approx 0.9\,\mathrm{MHz}$, with respect to the free pulsation value, $f_0 \approx 1.1\,\mathrm{MHz}$ predicted by linear analysis [21]; see also Eq. (15) for an analytical prediction. Repeating the frequency sweep for a lower initial distance, $z_{c0} = 2$, while fixing the sound amplitude to the same low value, i.e., $\varepsilon = 0.5$, so that shape pulsations affect only marginally the dynamic response, a further reduction was registered, $f_0 \approx 0.8\,\mathrm{MHz}$. This trend of decreasing resonance frequency as the distance from the wall decreases is in agreement with previous linear analysis for bubbles without elastic coating that interact with another bubble of similar size or a nearby rigid wall [12,13] as well as experimental findings [40].

In order to assess the effect of sound amplitude on the motion of the microbubble in the vicinity of a rigid wall we repeat the simulations for smaller sound amplitudes, i.e., $\varepsilon = 1$ and 1.7, and a shorter initial distance $z_{c0} = 2$ in order to minimize computational cost. The dynamic response pattern that is obtained in this fashion is illustrated in Fig. 11 indicating a similar trend as in Figs. 6 and 10, especially regarding the time evolution of the shape mode decomposition which is dominated by P_2 and P_3 in the manner previously described. Furthermore, the average speed of the bubble center of mass tends to increase for increasing sound amplitude. More specifically, the Bjerknes force depends quadratically on the sound amplitude; see also Eq. (30). In addition—and provided the translational Reynolds remains relatively small, $\mathrm{Re}_T \sim 1$—the viscous drag force that balances Bjerknes forces varies linearly with the translational velocity, Eq. (31), which in its turn increases quadratically with the sound amplitude, ε or δ_o in terms of the radial pulsation. This is corroborated by numerical evaluation of the translational speed slightly before trapping is achieved or by inspection of the time evolution of the average amplitude of P_1 shown in Figs. 10(b), 11(b), and 11(d). Regarding the evolution of the bubble shape in both cases it is seen to behave in the same manner as in the cases for larger amplitude and initial distance. In particular, the bubble exhibits two almost distinct phases where its center of mass is accelerated and decelerated while exhibiting prolate and oblate shapes, respectively. In the acceleration phase the dominant force balance is provided by Eqs. (30) and (31) denoting the equilibrium between the Bjerknes force and viscous drag, hence the prolate shape as a result of excess compression in the equator region where viscous shell stresses are negligible in comparison with elastic compressive stresses, as was already discussed in the previous subsection. As the microbubble reaches within a distance from the wall that is on the order of its radius the speed of its center of mass is decelerated due to the action of elastic lubrication pressure that develops at the axis of symmetry in the wall vicinity, in response to which the bubble deforms and flattens. As a result pressure drag replaces viscous drag in counteracting Bjerknes force thus facilitating the onset of oblate shapes that become progressively more pronounced as the magnitude of the Bjerknes force increases. This pattern is clearly registered in the panels of Figs. 6–11 illustrating the bubble shape during the phase of the bubble motion that can be described as trapped pulsation. Nevertheless, the pattern of trapped pulsation is not analyzed here and a thorough treatment of it is left for a separate study.

Focusing on the accelerating phase of the microbubble and based on a number of simulations that were performed for a wide parameter range we collect the shapes obtained as a result of the balance between Bjerknes forces and viscous drag at the time instant of maximum compression and plot them in order to assess the shape evolution as the speed of approach or elastic shell properties increases, Fig. 12. Ryskin and Leal [15] have constructed a collective graph on the Re_T, We_T plane for the case of a steadily rising bubble with $\mathrm{Re}_T \equiv \frac{\rho U 2R_0}{\mu} \leqslant 10$, $\mathrm{We}_T = \frac{2R_0U^2\rho}{\sigma} < 1$, and thus showed that the shape changes from spherical to an oblate ellipsoid as We_T increases for fixed Re_T. Our simulations show a different trend with the bubble shape changing from spherical to prolate, mostly during compression, since the force balance that determines the bubble shape is different. This behavior was recovered as the average translational velocity U increases for a range of not very large translational Reynolds $\mathrm{Re}_T \leqslant 10$ and modified $\mathrm{We}_T \equiv \frac{2R_0U^2\rho}{\chi}$ number, based on the shell area

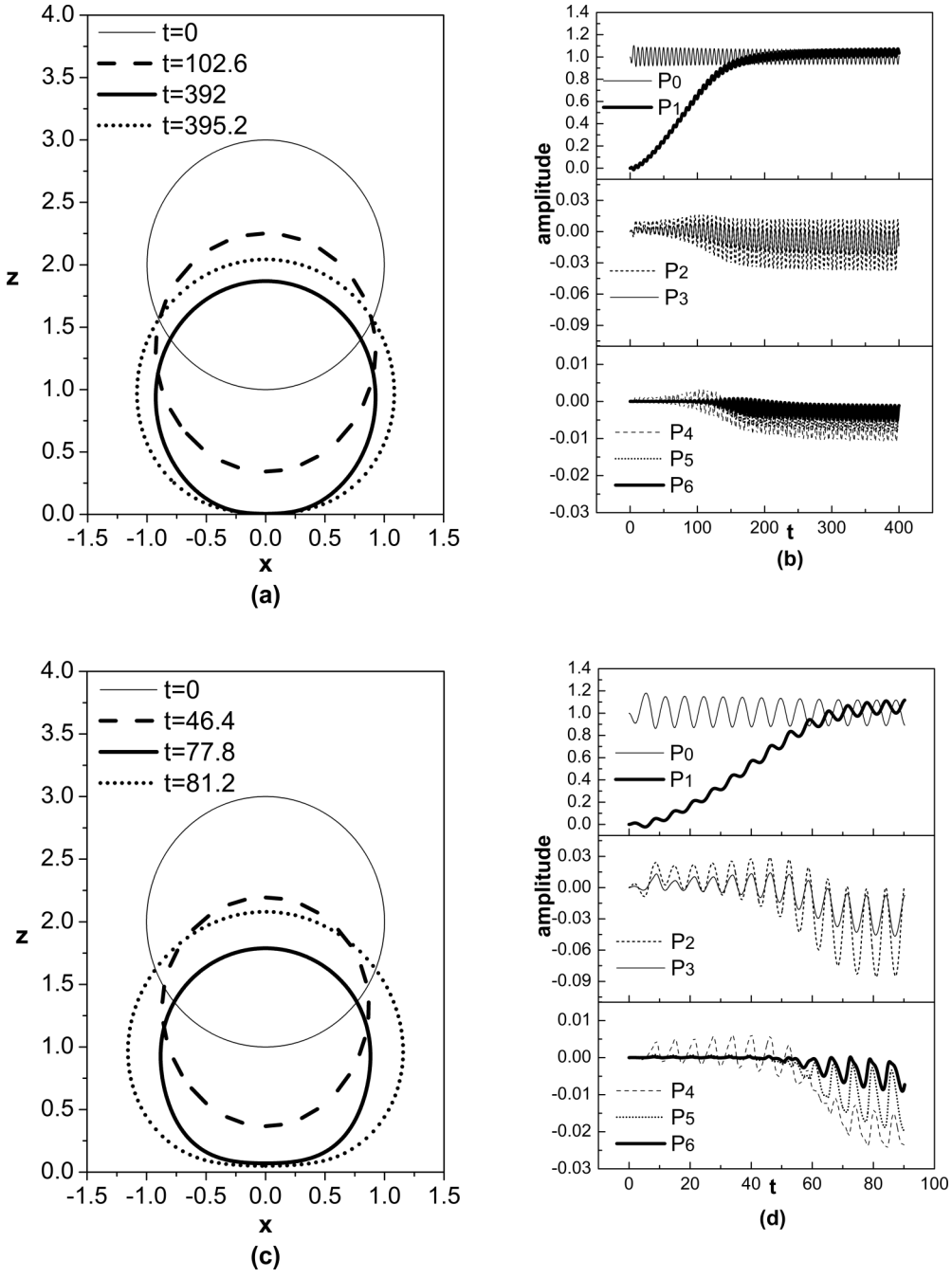

FIG. 11. Temporal evolution of (a,c) bubble shape; (b,d) breathing, P_0; translational P_1 modes; and shape mode decomposition, when the sound amplitude ε is set to 1.and 1.7, respectively: the initial bubble radius is $R_0 = 3.6\,\mu$m; shell properties are $\mu_s = 60 \times 10^{-9}$ kg/s, $\chi = 0.24$ N/m, and $k_B = 3 \times 10^{-14}$ N m; the initial distance from the wall is set to $z_{c0} = 2$; an acoustic disturbance of forcing frequency $f = 1.7$ MHz is imposed.

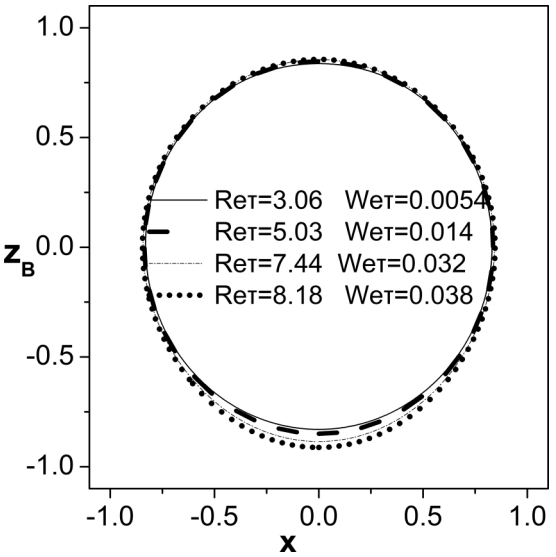

FIG. 12. Prolate shapes during compression for gradually increasing Re_T and We_T numbers of the translating microbubble.

dilatation modulus, as long as the microbubble remains relatively far from the wall, e.g., $z_c \geqslant 2$, in terms of the dimensionless distance between the bubble center of mass and the wall. In fact as We_T increases the amplitude of mode P_2 in the final shape also increases and the prolate shape obtained in the simulation becomes more pronounced; Fig. 12 provides a comprehensive view of these trends in a manner that is similar to the tendency shown in Fig. 9(a). However, the We_T numbers in our case are relatively small compared to the ones in [15] and thus the shapes are not as highly deformed. Nevertheless, the pattern of increased viscous drag with increasing translational velocity captured in Fig. 9 persists. In addition, intensification of viscous shell stresses is registered, as the pole region that faces the wall is approached from the bulk from the shell, as a manifestation of the tangential stress balance on the shell. The normal force balance is also affected in the south pole region, with the onset of viscous shell stresses partly accommodating the liquid overpressure while attenuating the elastic strain, thus leading to a gradual intensification of the prolate structure of the microbubble shapes.

It should, also, be stressed that the microbubble that is studied here is coated with an elastic shell and consequently has a nonslip interface with the surrounding liquid. As a result its dynamic response is closer to that of an oscillating solid sphere than to that of a pulsating bubble. In the former case simulations show that the drag coefficient c_D is not in accord with Levich's prediction for a translating bubble with a free surface [11], i.e., $c_D \approx 48/\mathrm{Re}$, as was recovered numerically by Ryskin and Leal [15] and in the earlier experimental study by Crum [10]; both studies treated bubbles with a free surface. Rather, it agrees with predictions for an oscillating rigid sphere proposed elsewhere [16,17], as illustrated in Fig. 13 for the relevant range of Re_T. Points on the latter graph were obtained by numerical evaluation of the drag coefficient via Eq. (30) over a wide range of shell and acoustic disturbance parameters, on the assumption that the equilibrium shape is produced as a result of the instantaneous balance between Bjerknes force and viscous drag. In order to minimize computational time numerical calculation of c_D was performed for an initial position of the center of mass z'_{c0} set to $2R_0$, subsequent numerical evaluation of radial amplitude δ_0, and average translational velocity $\langle U' \rangle$ for a wide range of shell and sound parameters and substitution in Eq. (30). The correlation shown in Eq. 1(c) provides the continuous curve in Fig. 13 and it is seen that it captures the numerically obtained dependence of c_D on Re_T for the entire parameter

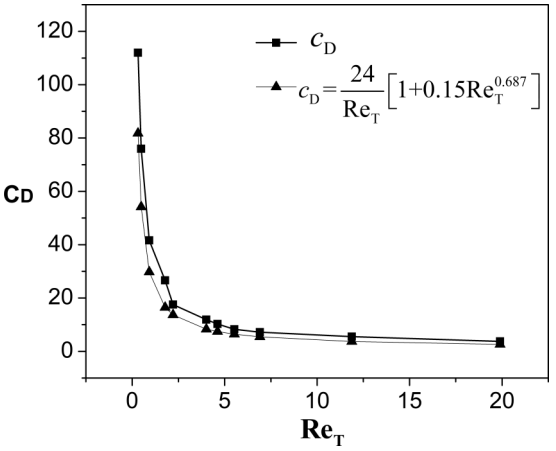

FIG. 13. Comparison between the drag coefficient for the microbubble translational motion as a function of the translational Reynolds number, Re_T, based on the average translational velocity of its center of mass, as obtained via application of Eq. (30) on the numerically obtained bubble average radial and translational velocity, and via the correlation in Eq. (31) provided in [17].

range employed in the present study, provided the bubble has not reached the vicinity of the wall, $z_c > 1$. In other words, the force balance described by Eqs. (30) and (31) remains valid, as long as the shape of the pulsating and translating bubble microbubble does not exhibit significant variations from sphericity and this is true for the biggest part of the simulation, as illustrated by Figs. 6–12 in panels illustrating the shape evolution and shape mode decomposition, and discussed in the context of Fig. 8. This assumption loses validity as the bubble performs trapped pulsations near the wall, in which case proximity with the rigid wall and the resulting pressure drag unavoidably cause flattening of the protective shell [Figs. 6(c), 9(a), 10(a), and 11(a)] and the onset of oblate shapes. Furthermore, the onset of parametric shape mode excitation produces bending stresses that result in large curvature variation. The latter effect emerges irrespective of the presence of the wall provided a certain threshold in amplitude of the acoustic excitation is exceeded, for given shell parameters and forcing frequency [21], but the onset of shape modes is accelerated due to the wall presence.

V. CONCLUSIONS

In the present study we numerically investigate the dynamic response of an encapsulated microbubble in a wall restricted flow due to an acoustic disturbance in the far field pressure, when viscous and inertia forces in the surrounding fluid and viscoelastic stresses in the protective shell are accounted for. Coupling a superparametric finite element methodology with an elliptic mesh generation scheme allowed us to capture the dynamic response of coated microbubbles as they accelerate towards the wall, until trapping is achieved in the form of a steady pulsation at a very low average distance from the wall.

In the presence of the wall the bubble is seen to perform volume pulsations while translating in its vicinity due to the secondary Bjerknes force. As the distance from the wall decreases the resonance frequency of the microbubble pertaining to volume pulsation also decreases, as is the case with conventional bubbles without elastic coating. Furthermore, the microbubble gradually accelerates towards the wall with a velocity that is produced by the almost instantaneous equilibrium between Bjerknes forces and viscous drag from the surrounding liquid. This is a result of the fast damping of the volume pulsations effected by shell viscosity that reduces the streaming and translational Reynolds numbers and therefore minimizes the importance of the history force in

the bubble translation. The calculated drag coefficient conforms with experimental measurements and relevant correlations for nonslip surfaces [16,17], $c_D = \frac{24}{\mathrm{Re}_T}[1 + 0.15\mathrm{Re}_T^{0.687}]$, and the velocity depends nearly quadratically on the sound amplitude and the distance from the wall, in agreement with relevant experimental and theoretical studies with conventional bubbles [10,13]; see also Eqs. (30) and (31).

Translation towards the wall takes place mostly during volume compression, due to the reduced added mass of the bubble. During this phase of the pulsation large viscous stresses are generated from the surrounding liquid in the region around the equator, where the tangential velocity of the interface acquires a maximum that resists the translation of the bubble. As a result, the tangential force balance produces compressive viscous shell stresses that gradually increase as the pole region that faces towards the wall is approached. The onset of the viscous shell stresses attenuate the elastic strain that is required to balance liquid overpressure in the same pole region, and this results in the prolate shape exhibited by the microbubble in the simulations during the acceleration phase of its motion, in agreement with experimental observations [7,8]. This is in contrast to the behavior exhibited by free bubbles that exhibit oblate shapes when they rise due to buoyancy [15], and is a result of the fact that it is viscous drag rather than pressure drag that balances the driving force of the motion, i.e., Bjerknes force and buoyancy in the situation examined in the present study and in the case of rising bubbles, respectively.

At the same time parametric shape mode excitation was captured beyond a sound amplitude threshold that was determined by previous stability analysis in the absence of wall interaction and ignoring viscous dissipation in the surrounding liquid, assuming that the bubble shape remains spherical [21]. The presence of the wall tends to modify this pattern but the above threshold remains a reliable marker of stability. Once the sound amplitude was raised beyond this threshold the bubble surface was seen to be rapidly destabilized, mostly when it achieved maximum compression. Jet formation was not captured through the bubble interface as the sound amplitude increased since bending resistance and viscosity of the shell prevented excessive bending in the region around the north pole that faces away from the wall, in agreement with previous findings for coated microbubbles [23]. Rather, the bubble loses coherence via growth of shape modes throughout its interface with the surrounding liquid. Provided we remain below the above threshold for severe shape mode excitation to take place, the microbubble accelerates and eventually reaches the wall where its motion is halted due to the onset of elastolubrication pressure. During this phase of its motion it acquires an oblate shape and performs steady pulsations trapped by the wall which will be examined in detail in an ensuing article.

Finally, the relative contribution to energy dissipation due to bulk liquid and shell viscosity was examined and it was shown that even though shell damping always dominates over dissipation due to liquid viscosity, the assumption of potential flow starts losing validity as the microbubble approaches a nearby boundary.

ACKNOWLEDGMENTS

This research has been carried out within the framework of the invitation "Expression of interest for holders of doctoral diploma, for scholarship for postdoctoral research" of the University of Thessaly which is implemented by the University of Thessaly and is funded by the Stavros Niarchos Foundation. We also acknowledge for financial support at the early stages of this work given by the operational program "Education and lifelong learning"-"Aristeia I-CONTAGEUSNUMSTADY/1509", which was cofounded by the European Union (European Social Fund) and national resources.

APPENDIX: ENERGY DISSIPATION

An interesting issue that needs to be addressed in the present study pertains to the validity of the potential flow assumption when studying the dynamic response of contrast agents in the vicinity of

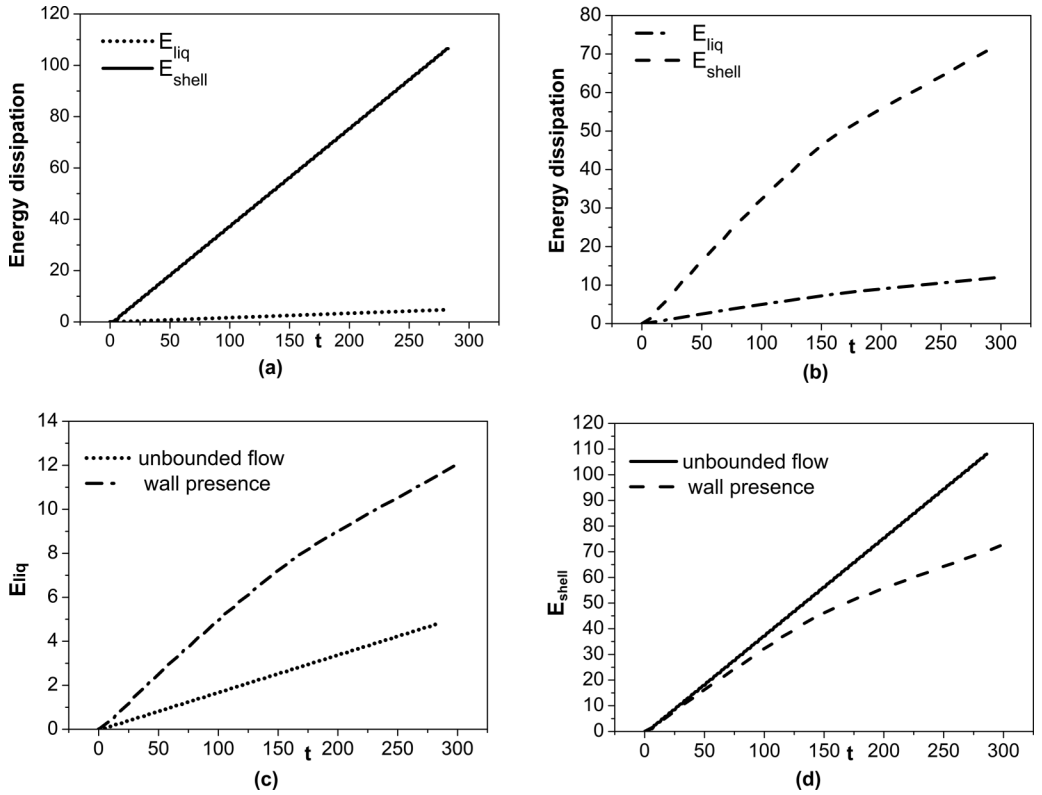

FIG. 14. (a), (b) Temporal evolution of energy dissipation due to liquid viscosity, E_{liq}, and shell damping, E_{shell}, in an unbounded flow and in the vicinity of a wall, respectively; (c), (d) comparison of the evolution of E_{liq} and E_{shell}, respectively, in an unbounded flow and in the vicinity of a wall; the initial bubble radius is $R_0 = 3.6\,\mu$m; shell properties are $\mu_s = 60 \times 10^{-9}$ kg/s, $\chi = 0.24$ N/m, and $k_B = 3 \times 10^{-14}$ N m; the initial distance from the wall in wall bounded simulations is set to $z_{c0} = 4$; an acoustic disturbance of forcing frequency $f = 1.7$ MHz and sound amplitude $\varepsilon = 2$ are imposed.

a wall. By taking the scalar product of the velocity field $\boldsymbol{u}$ with the Navier-Stokes equation (4), the differential and dimensionless form of the mechanical energy balance is obtained [23]:

$$\frac{D(u^2/2)}{Dt} = \nabla \cdot (\underline{\underline{\sigma}} \cdot \boldsymbol{u}) + p\nabla \cdot \boldsymbol{u} - \frac{1}{\mathrm{Re}}\underline{\underline{\tau}} : \nabla \boldsymbol{u} = \nabla \cdot (\underline{\underline{\sigma}} \cdot \boldsymbol{u}) - \phi, \tag{A1}$$

where ϕ denotes the energy dissipation due to the liquid viscosity, i.e., the amount of irreversible conversion of mechanical energy into heat as a result of the fluid motion. Upon integration over the entire flow domain, application of the Gauss divergence theorem, and introduction of the interfacial force balance Eq. (5), the mechanical energy conservation equation is recovered in integral form:

$$\frac{D}{Dt}\iiint_V \frac{u^2}{2} dV = \iint_A \boldsymbol{u} \cdot \boldsymbol{\sigma}_n dA - \iiint_V \phi dV = \iint_{A_B} \boldsymbol{u} \cdot \left[\left(P_\infty - P_G + \frac{2k_m}{We}\right)\boldsymbol{n}_B - \boldsymbol{\Delta F}\right] dA - \Phi, \tag{A2}$$

where $\Phi = \iiint_V \phi dV$ signifies the total amount of irreversible transform of mechanical energy into heat within the control volume, $\boldsymbol{\sigma}_n = \boldsymbol{n} \cdot \underline{\underline{\sigma}}$ the stress vector at the bubble-liquid, A_B, and far field, A_∞, surfaces that enclose the control volume and $\boldsymbol{n}_B = -\boldsymbol{n}$ with $\boldsymbol{n}$ pointing towards the flow interior. The integral on the right-hand side of Eq. (A2) provides the rate of change of the compression,

surface, strain, and bending energy [12,13,19]:

$$\begin{aligned}
&\frac{D}{Dt}\left\{\iiint_V \frac{u^2}{2}dV + \frac{1}{\mathrm{We}}\iint_{A_B} dA + V\left(P_\infty + \frac{P_g}{\gamma-1}\right) + \iint_{A_{B0}} W_S dA_0 + \iint_{A_{B0}} W_B dA_0\right\} \\
&\quad = -\Phi - \iint_{A_B} \boldsymbol{u}\cdot\boldsymbol{\Delta F}_v dA \rightarrow \left\{\iiint_V \frac{u^2}{2}dV + \frac{1}{\mathrm{We}}\iint_{A_B} dA + V\left(P_\infty + \frac{P_g}{\gamma-1}\right)\right. \\
&\qquad \left. + \iint_{A_{B0}} W_S dA_0 + \iint_{A_{B0}} W_B dA_0\right\}\Big|_t \\
&\quad = \frac{1}{\mathrm{We}}\iint_{A_{B0}} dA + V_0\left(P_\infty + \frac{P_{g0}}{\gamma-1}\right) - \int_0^t \Phi dt - \int_0^t \left(\iint_{A_B} \boldsymbol{u}\cdot\boldsymbol{\Delta F}_v dA\right)dt - \varepsilon P_{\mathrm{st}}\int_0^t \sin tV\, dt,
\end{aligned} \tag{A3}$$

with A_{B0}, V_0, and P_{G0} signifying the undeformed interfacial area, the volume, and initial pressure of the microbubble; W_s and W_B the strain and bending energy of the shell per unit undeformed bubble area; and $\boldsymbol{\Delta F}_V$ the part of the interfacial forces that arise as a result of shell viscosity.

Therefore, by calculating the integrals $E_{\mathrm{liq}} = \int_0^t \Phi dt$ and $E_{\mathrm{shell}} = \int_0^t (\iint_{A_B} \boldsymbol{u}\cdot\boldsymbol{\Delta F}_v dA)dt$ of Eq. (A3) as time evolves, we follow the temporal evolution of the dissipation in the bulk of the flow and due to shell damping, respectively. In Fig. 14(a) the case of the contrast agent employed in Fig. 6 is shown as it pulsates in an unbounded flow under an acoustic disturbance of frequency 1.7 MHz and an amplitude $\varepsilon = 2$. Clearly, throughout the simulation shell damping is more significant than liquid dissipation, which justifies the assumption of potential flow in studies focusing in contrast agents located away from boundaries. When the same simulation is repeated for a wall bounded flow, Fig. 14(b), the same pattern is reported with shell damping dominating over viscous dissipation in the bulk of the liquid. In fact, as the bubble reaches closer to the wall, an increase in bulk viscous dissipation is recorded that becomes more significant compared to the unbounded flow [Fig. 14(c)], whereas shell damping is reduced, Fig. 14(d). Therefore, the assumption of potential flow starts to lose validity when the bubble interacts with a nearby wall and extra attention is needed to determine conditions for which viscous forces of the surrounding liquid may be neglected.

[1] B. A. Kaufmann, K. Wei, and J. R. Lindner, Contrast echocardiography, Curr. Probl. Cardiol. **32**, 51 (2007).

[2] K. Efthymiou, N. Pelekasis, M. B. Butler, D. H. Thomas, and V. Sboros, The effect of resonance on transient microbubble acoustic response: Experimental observations and numerical simulations, J. Acoust. Soc. Am. **143**, 1392 (2018).

[3] K. Ferrara, R. Pollard, and M. Borden, Ultrasound microbubble contrast agents: Fundamentals and application to gene and drug delivery, Annu. Rev. Biomed. Eng. **9**, 415 (2007).

[4] Y. Taniyama, K. Tachibana, K. Hiraoka, T. Namba, K. Yamasaki, N. Hashiya, M. Aoki, T. Ogihara, K. Yasufumi, and R. Morishita, Local delivery of plasmid DNA into rat carotid artery using ultrasound, Circulation **105**, 1233 (2002).

[5] P. Marmottant and S. Hilgenfeldt, Controlled vesicle deformation and lysis by single oscillating bubbles, Nature **423**, 153 (2003).

[6] A. A. Doinikov and A. Bouakaz, Effect of a distant rigid wall on microstreaming generated by an acoustically driven gas bubble, J. Fluid Mech. **742**, 425 (2014).

[7] H. J. Vos, B. Dollet, J. G. Bosch, M. Versluis, and N. de Jong, Nonspherical vibrations of microbubbles in contact with a wall: A pilot study at low mechanical index, Ultrasound Med. Biol. **34**, 685 (2008).

[8] S. Zhao, K. W. Ferrara, and P. A. Dayton, Asymmetric oscillation of adherent targeted ultrasound contrast agents, Appl. Phys. Lett. **87**, 134103 (2005).

[9] H. Chen, W. Kreider, A. A. Brayman, M. R. Bailey, and T. J. Matula, Blood Vessel Deformations on Microsecond Time Scales by Ultrasonic Cavitation, Phys. Rev. Lett. **106**, 034301 (2011).
[10] L.A. Crum, Bjerknes forces on bubbles in a stationary sound field, J. Acoust. Soc. Am. **57**, 1363 (1975).
[11] D. W. Moore, The velocity of rise of distorted gas bubbles in a liquid of small viscosity, J. Fluid Mech. **23**, 749 (1965).
[12] N. Pelekasis and J. Tsamopoulos, Bjerknes forces between two bubbles. Part 1. Response to a step change in pressure, J. Fluid Mech. **254**, 467 (1993).
[13] N. Pelekasis and J. Tsamopoulos, Bjerknes forces between two bubbles. Part 2. Response to an oscillatory pressure field, J. Fluid Mech. **254**, 501 (1993).
[14] G. Ryskin and L. G. Leal, Numerical solution of free-boundary problems in fluid mechanics. Part 1. The finite-difference technique, J. Fluid Mech. **148**, 1 (1984).
[15] G. Ryskin and L.G. Leal, Numerical solution of free-boundary problems in fluid mechanics. Part 2. Buoyancy-driven motion of a gas bubble through a quiescent liquid, J. Fluid Mech. **148**, 19 (1984).
[16] R. Clift, J. R. Grace, and M. E. Weber, *Bubbles, Drops, and Particles* (Academic Press, New York, 1978).
[17] R. Mei, Flow due to an oscillating sphere and an expression for unsteady drag on the sphere at finite Reynolds number, J. Fluid Mech. **270**, 133 (1994).
[18] S. Qin and K. W. Ferrara, Acoustic response of compliable microvessels containing ultrasound contrast agents, Phys. Med. Biol. **51**, 5065 (2006).
[19] K. Tsiglifis and N. Pelekasis, Simulations of insonated contrast agents: Saturation and transient break-up, Phys. Fluids **25**, 032109 (2013).
[20] Y. Liu, K. Sugiyama, S. Takagi, and Y. Matsumoto, Numerical study on the shape oscillation of an encapsulated microbubble in ultrasound field, Phys. Fluids **23**, 041904 (2011).
[21] K. Tsiglifis and N. Pelekasis, Parametric stability and dynamic buckling of encapsulated microbubble subject to acoustic disturbances, Phys. Fluids **23**, 012102 (2011).
[22] M. Koch, Ch. Lechner, F. Reuter, K. Kohler, R. Metting, and W. Lauterborn, Numerical modeling of laser generated cavitation bubbles with the finite volume and volume of fluid method, using OpenFOAM, Comput. Fluids **126**, 71 (2016).
[23] M. Vlachomitrou and N. Pelekasis, Dynamic simulation of a coated microbubble in an unbounded flow: Response to a step change in pressure, J. Fluid Mech. **822**, 717 (2017).
[24] C. C. Church, The effects of an elastic solid surface layer on the radial pulsations of gas bubbles, J. Acoust. Soc. Am. **97**, 1510 (1995).
[25] D. B. Khismatullin and A. Nadim, Radial oscillations of encapsulated microbubbles in viscoelastic liquids, Phys. Fluids **14**, 3534 (2002).
[26] K. Sarkar, W. T. Shi, D. Chatterjee, and F. Forsberg, Characterization of ultrasound contrast microbubbles using *in vitro* experiments and viscous and viscoelastic interface models for encapsulation, J. Acoust. Soc. Am. **118**, 539 (2005).
[27] P. Marmottant, S. van der Meer, M. Emmer, M. Versluis, N. de Jong, S. Hilgenfeldt, and D. Lohse, A model for large amplitude oscillations of coated bubbles accounting for buckling and rupture, J. Acoust. Soc. Am. **118**, 3499 (2005).
[28] S. Timoshenko and S. Woinowsky-Krieger, *Theory of Plates and Shells* (McGraw-Hill, New York, 1959).
[29] C. Pozrikidis, Effect of membrane bending stiffness on the deformation of capsules in simple shear flow, J. Fluid Mech. **440**, 269 (2001).
[30] D. Barthes-Biesel, A. Diaz, and E. Dhenin, Effect of constitutive laws for two-dimensional membranes on flow-induced capsule deformation, J. Fluid Mech. **460**, 211 (2002).
[31] K. Tsiglifis and N. Pelekasis, Nonlinear radial oscillations of encapsulated microbubbles subject to ultrasound: The effect of membrane constitutive law, J. Acoust. Soc. Am. **123**, 4059 (2008).
[32] R. Mettin, I. Akhatov, U. Parlitz, C. D. Ohl, and W. Lauterborn, Bjerknes forces between small cavitation bubbles in a strong acoustic field, Phys. Rev. E **56**, 2924 (1997).
[33] Y. Saad and M. H. Schultz, GMRES: A generalized minimal residual algorithm for solving non-symmetric linear systems, SIAM J. Sci. Stat. Comput. **7**, 856 (1986).
[34] Y. Saad, *Iterative Methods for Sparse Linear Systems* (Society for Industrial and Applied Mathematics, Philadelphia, 1996).

[35] Y. Dimakopoulos and J. Tsamopoulos, A quasi-elliptic transformation for moving boundary problems with large anisotropic deformations, J. Comput. Phys. **192**, 494 (2003).

[36] K. N. Christodoulou and L. E. Scriven, Discretization of free surface flows and other moving boundary problems, J. Comput. Phys. **99**, 39 (1992).

[37] K. Tsiveriotis and R. A. Brown, Boundary-conforming mapping applied to computations of highly deformed solidification interfaces, Int. J. Numer. Methods Fluids **14**, 981 (1992).

[38] N. Chatzidai, A. Giannousakis, Y. Dimakopoulos, and J. Tsamopoulos, On the elliptic mesh generation in domains containing multiple inclusions and undergoing large deformations, J. Comput. Phys. **228**, 1980 (2009).

[39] B. Dollet, S. M. van der Meer, V. Garbin, N. de Jong, D. Lohse, and M. Versluis, Nonspherical oscillations of ultrasound contrast agent microbubbles, Ultrasound Med. Biol. **34**, 1465 (2008).

[40] A. Vogel and W. Lauterborn, Acoustic transient generation by laser-produced cavitation bubbles near solid boundaries, J. Acoust. Soc. Am. **84**, 719 (1988).